THE ASTROPHYSICAL JOURNAL, 366:141–162, 1991 January 1

CO $J = 3 \rightarrow 2$ OBSERVATIONS OF TRANSLUCENT AND HIGH-LATITUDE MOLECULAR CLOUDS[1]

EWINE F. VAN DISHOECK
Division of Geological and Planetary Sciences, California Institute of Technology
JOHN H. BLACK
Steward Observatory
T. G. PHILLIPS
Division of Physics, Mathematics and Astronomy, California Institute of Technology
AND
R. GREDEL
European Southern Observatory
Received 1990 April 25; accepted 1990 June 25

ABSTRACT

Measurements of the CO $J = 3 \rightarrow 2$ emission line at 345 GHz in translucent and high-latitude clouds are reported. Together with data on the $J = 2 \rightarrow 1$ and $J = 1 \rightarrow 0$ lines of both ^{12}CO and ^{13}CO, they are used to constrain the densities in the clouds. The physical conditions in the high-latitude clouds are found to be very similar to those in the translucent clouds. The CO emission-line data complement optical absorption-line observations of the C_2 molecule in the same region, which provide independent constraints on temperature and density. The densities derived from the ^{12}CO $1 \rightarrow 0/3 \rightarrow 2$ ratios are often higher than those inferred from the C_2 excitation, whereas densities derived from the $3 \rightarrow 2/^{13}CO$ $1 \rightarrow 0$ ratios are found to be very similar to those based on C_2. Several explanations for these differences are discussed, including the possibility that the CO and C_2 molecules are distributed differently throughout a cloud. Various "clumpy" cloud models have been developed to explore this question. No CO $J = 3 \rightarrow 2$ emission has been detected from the classical diffuse cloud toward ζ Oph. The very low limit, $T_A^*(3 \rightarrow 2) \leq 0.08$ K, excludes high-density ($n_H > 700$ cm^{-3}) models for this line of sight. Evidence is found for a slight decrease in the $J = 1 \rightarrow 0/3 \rightarrow 2$ and $2 \rightarrow 1/3 \rightarrow 2$ line intensity ratios from the edge to the center of one cloud, which can be explained by a corresponding increase in the density into the center. The CO lines often show complex profiles consisting of several narrow ($\Delta V \leq 1$ km s^{-1}) components; in some cases the profiles show centrally reversed line cores that can be interpreted in terms of gradients in density, temperature, and molecular abundance within a single kinematic component.

Subject headings: high-latitude objects — interstellar: molecules

I. INTRODUCTION

Translucent and high-latitude molecular clouds with $A_V^{tot} \approx$ 1–5 mag have attracted considerable attention in recent years, through observations at both optical and millimeter wavelengths. Not only are these clouds interesting as a class by themselves, but they also provide the important link between the classical diffuse and dense interstellar clouds. A major distinction between thin, diffuse clouds and thick, dense clouds is the extent to which ultraviolet photoprocesses control the chemistry and ionization. Indeed, there is growing evidence that dense molecular clouds have a very clumpy structure through which the ultraviolet radiation can penetrate (e.g., Stutzki *et al.* 1988); the clumps are estimated to be similar in size to the translucent clouds, so that a detailed study of their structure and chemistry is quite relevant to the study of dense clouds.

At optical wavelengths, about 25 translucent clouds have been observed through absorption lines of molecules like CH, C_2, CN, and CH^+ toward bright stars located fortuitously behind the clouds (Crutcher 1985; see van Dishoeck and Black 1988*a*, 1989 for overviews). More recently, these molecules have also been detected toward a number of stars located behind high-latitude clouds (de Vries and van Dishoeck 1988*a*, *b*; Welty *et al.* 1989; Penprase *et al.* 1990). Absorption-line studies not only provide molecular abundances but also put constraints on the distance to the cloud (Hobbs, Blitz, and Magnani 1986; Hobbs *et al.* 1988) and can give information on the extinction and other properties of the dust. At millimeter wavelengths, the observations have until now focused on the nearby ($d \approx 100$ pc) high-latitude clouds, which have the advantage over most low-latitude translucent clouds that they are free of potentially confusing background emission (Magnani, Blitz, and Mundy 1985; Keto and Myers 1986). Observations of ^{12}CO and ^{13}CO provide direct measures of the size, morphology, and kinematics of the cloud, as well as indirect estimates of the total column density and mass of hydrogen. The weak ($T_A^* \approx 0.5$–4 K) $J = 1 \rightarrow 0$ lines of ^{12}CO and ^{13}CO from nearby translucent and high-latitude clouds are, at worst, slightly saturated and can thus reveal structure on small scales. The millimeter-wavelength emission-line data typically refer to a beam size of about 30″, which corresponds to 6000 AU at 200 pc. For comparison, optical absorption-line measurements sample scales that are governed by the angular size of the background star, which is only 0.04 AU at 200 pc seen toward a 10 $R_\odot$ star at 500 pc. On the other hand, velocity

[1] Based in part on observations collected at the European Southern Observatory, La Silla, Chile.

resolution of 0.1 km s^{-1} or better can routinely be achieved at millimeter wavelengths, but the resolution is usually 3 km s^{-1} or worse for the optical measurements.

Detailed models of the depth-dependent structure and chemistry in translucent and high-latitude clouds have been developed by van Dishoeck and Black (1986*a*, 1988*b*, 1989) and by Viala (1986) and coworkers (Viala *et al.* 1988*a*). The models incorporate the latest laboratory data on the important, but complicated, photodissociation of CO and its isotopes (Letzelter *et al.* 1987; Stark *et al.* 1990) and make predictions about the abundances and excitation of other species. The results depend strongly on the adopted physical parameters in the cloud, such as density, temperature, and strength of the incident ultraviolet radiation field. For the classical diffuse clouds studied with the *Copernicus* satellite, these properties can be inferred from a number of diagnostic observations. However, as illustrated in Table 1 of van Dishoeck (1990), the relevant ultraviolet data are lacking for the more recently discovered translucent and high-latitude clouds. In particular, no high-resolution ultraviolet observations of the rotational excitation of H_2 and the fine-structure excitation of C, C^+, and O have been obtained prior to the launch of the *Hubble Space Telescope*. The only diagnostic available through ground-based absorption line observations is the C_2 molecule. The C_2 rotational populations result from the competition between collisional excitation and deexcitation processes, and radiative pumping at far-red wavelengths, $\lambda \approx 1$ μm (van Dishoeck and Black 1982). The populations of the lowest J levels are sensitive to the temperature in the cloud, whereas those of the higher J levels depend on the combination of parameters $n\sigma_0/I_R$, where $n = n(\mathrm{H}) + n(\mathrm{H_2})$ is the density of collision partners, σ_0 is the collisional cross section, and I_R is the scaling factor for the radiation field at far-red wavelengths. Owing to uncertainties in the C_2 collisional cross sections and in the strength of the interstellar radiation field at $\lambda \approx 1$ μm, the inferred densities are uncertain by factors of a few.

The CO molecule may be particularly suited to provide independent measurements of the density in these clouds. The molecule is abundant and has a small dipole moment. Its excitation in translucent and high-latitude clouds is therefore dominated by collisions with neutral species, rather than by electrons. Owing to rapid improvements in the sensitivity of high-frequency detectors, it is now possible to observe lines as weak as 0.1 K in the 345 GHz window in reasonable amounts of integration time. We report here measurements of the CO $J = 3 \rightarrow 2$ emission from a number of translucent and high-latitude clouds, and use them, together with CO $J = 1 \rightarrow 0$ and $2 \rightarrow 1$ observations, to constrain the densities in the clouds. In particular, it will be interesting to see whether there are any significant differences in the physical properties of the translucent and high-latitude clouds. The densities are compared with those inferred from the C_2 excitation, wherever possible.

II. OBSERVATIONS

a) Submillimeter and Millimeter Observations

The CO $J = 3 \rightarrow 2$ observations at 345.796 GHz were performed at the Caltech Submillimeter Observatory (CSO) in 1988 July, 1989 March and October and 1990 March. During the 1988 July run, the telescope was equipped with the Berkeley 345 GHz liquid helium–cooled SIS receiver in the sidecab, with a double-sideband receiver temperature of about 400 K (Sutton *et al.* 1990). The backend was an acousto-optical spectrometer (AOS) consisting of 1000 channels over a 500 MHz bandwidth (Masson 1982). The effective resolution was about 1.6 km s^{-1}, somewhat coarser than the channel width of 0.43 km s^{-1}. In 1989 March, the new Caltech 345 GHz SIS receiver (Ellison *et al.* 1989) mounted at the Cassegrain focus was used, in conjunction with the same low-resolution backend. The double-sideband receiver temperature was typically 250–300 K during this run but improved to less than 200 K during subsequent runs. For the 1989 October and 1990 March observations, the Caltech 345 GHz SIS receiver was connected to a new high-resolution AOS with a 50 MHz bandwidth and an effective resolution of 0.043 km s^{-1}. The weather conditions during the first two runs and during the 1990 March run were reasonable to good for observations at 345 GHz, but poor in 1989 October. In 1989 March and October, some positions were also observed in the CO $J = 2 \rightarrow 1$ line at 230.537 GHz with the Caltech 230 GHz SIS receiver. During the last observing run, this receiver had a noise temperature of less than 100 K. All spectra were taken in position-switching mode. Offset positions were chosen either on the basis of CO $J = 1 \rightarrow 0$ maps, or by switching by 1°–2° in azimuth. The beam sizes of the CSO are measured to be 20″ at 345 GHz and 32″ at 230 GHz, full width at half-maximum.

In order to compare the CO $J = 3 \rightarrow 2$ data with the $2 \rightarrow 1$ and $1 \rightarrow 0$ data, accurate calibration is required. At the CSO, the calibration is performed using the chopper-wheel method (Penzias and Burrus 1973). The resulting antenna temperatures are denoted T_A^* and have not yet been corrected for the cold spillover efficiency and the efficiency with which the antenna beam couples to the source. Since the clouds studied in this work are often extended compared with the beam size, the efficiency correction factor for these two effects has been determined from observations of an extended source, such as the full Moon. The resulting Moon-beam efficiency factors were 0.68 (Berkeley 345 GHz receiver), 0.74 (Caltech 345 GHz receiver), and 0.77 (Caltech 230 receiver). These factors are 10%–25% larger than the corresponding efficiencies for sources that are small compared with the beam size. The overall uncertainties in the calibration are estimated to be of the order of 30%. Whenever possible, strong sources such as Orion, IRC +10216, and NGC 7027 were observed throughout the night to check that the relative variations in the calibration were less than 15%. In addition, most sources were observed during at least two observing runs with different equipment. The corresponding antenna temperatures generally agree to better than 30%. The intensities, corrected for cold spillover and coupling to an extended source, are presented as T_R, the Rayleigh-Jeans radiation temperature (Kutner and Ulich 1981).

CO $J = 1 \rightarrow 0$ data were collected from a variety of observatories. Part of them were obtained in 1988 October at the NRAO Kitt Peak 12 m telescope[2] with the 115 GHz SIS receiver, equipped with both low-resolution (250 kHz or 0.65 km s^{-1}) and high-resolution (30–100 kHz, or 0.08–0.26 km s^{-1}) filter banks. The calibration procedure at Kitt Peak corrects for the cold spillover efficiency, so that the resulting spectra are presented in terms of T_R^*. For extended sources, the coupling efficiency is assumed to be unity (P. Jewell 1989, private communication). Additional observations were collected throughout the year at the 15 m Swedish-ESO Submillimeter Telescope (SEST) in Chile with the 115 GHz Schottky barrier

[2] The National Radio Astronomy Observatory is operated by Associated Universities, Inc., under contract with the National Science Foundation.

diode receiver and the high-resolution AOS backend (0.13 km s^{-1}). These data were recorded as T_A^*, and the Moon-beam efficiency has been measured to be 0.92. However, comparison of the SEST data with the Kitt Peak data for the same sources indicates that the SEST data are systematically lower by about 10%. The origin of this discrepancy is not understood, but for consistency, we have adopted a somewhat lower Moon-beam efficiency of 0.82 for the SEST data. Limited 230 GHz data were collected at SEST. At this frequency, the Moon-beam efficiency is approximately 0.75. The 115 and 230 GHz SEST data were taken in frequency-switching mode, whereas the Kitt Peak data were obtained with position switching. The uncertainties in calibration are estimated to be about 15%–20% for both telescopes. The beam sizes at 115 GHz are 55″ and 44″ for the Kitt Peak and SEST telescopes, respectively. Details of the SEST observations will be discussed elsewhere.

b) *Selection of Sources*

The translucent clouds were chosen from the list compiled by van Dishoeck and Black (1989). This sample was selected optically on the basis of strong interstellar absorption lines in the spectra of reddened stars. For most clouds, only the direction of the background star was observed in CO $J = 3 \rightarrow 2$. Limited maps were made in CO $J = 1 \rightarrow 0$ around the stellar position, and these will be discussed elsewhere (Gredel *et al.* 1990; Gredel, van Dishoeck, and Black 1990). In a few cases, the maps show significant structure on scales of a few arcminutes. However, except for one or two directions, no significant variation is found on scales of 20″–60″; therefore, comparison of data obtained with different beam sizes in this range is thought to be meaningful. The beam sizes correspond to scales of 0.015–0.15 pc at the estimated distances of these clouds,

TABLE 1

OBSERVED POSITIONS IN TRANSLUCENT AND HIGH-LATITUDE CLOUDS[a]

Star/Cloud	α(1950)	δ(1950)	C_2	OH	H_2CO	C_3H_2
HD 21389	03h25m54s.2	+58°42′26″.4	–	–	–	–
HD 21483	03 25 42.2	+30 12 12.4	–	–	–	–
HD 26571	04 09 53.1	+22 17 11.7	–	–	–	–
HD 29647	04 38 03.8	+25 53 50.3	+	–	–	–
HD 62542	07 40 58.1	−42 06 36.2	+	–	–	–
HD 73882	08 37 19.5	−40 14 31.6	+	–	–	–
HD 80077	09 14 13.3	−49 45 50.1	+	–	–	–
HD 147084	16 17 37.4	−24 03 02.0	+	–	–	–
HD 147889	16 22 22.8	−24 21 07.2	+	–	–	–
ζ Oph	16 34 24.1	−10 28 02.8	+	+	–	–
HD 154368	17 03 08.5	−35 23 05.1	+	–	–	–
BD −14° 5037	18 22 15.0	−14 40 41.2	+	–	–	–
HD 169454	18 22 24.9	−14 00 25.5	+	–	–	–
HD 210072	22 04 29.8	+55 00 09.6	–	–	–	–
α Ori 4	05 53 44	07 23 58	–	–	–	–
MBM 26A	08 04 00.0	61 22 00	–	–	+	–
MBM 32A	09 30 38.0	66 11 06	–	–	+	+
MBM 32B	09 28 42.0	66 05 00	–	+	–	–
MBM 32C	09 32 00.0	66 05 00	–	–	+	–
MBM 32D	09 28 42.0	66 09 00	–	–	–	–
MBM 40A	16 08 13.2	21 59 30	–	–	+	–
MBM 40B	16 08 15	22 01	–	–	–	–
MBM 40C	16 08 24	21 57	–	+	+	+
MBM 40D	16 07 46.4	22 09 28	–	–	*	+
MBM 53A	23 05 43	22 37	–	–	–	–
MBM 54A	23 06 48	18 13	–	–	–	–
MBM 55A	23 06	14 20	–	–	+	*
MBM 55B	23 05 54	14 45	–	–	–	–
MBM 55C	23 05 29	14 38	–	–	–	–
MBM 55D	23 05 54	14 49	–	+	+	+
HD 210121	22 05 36.1	−03 46 35.5	+	–	–	–
HD 210121 A	22 05 04	−03 56 35.5	–	–	–	–
HD 210121 B = B8	22 03 26.4	−03 46 35.5	–	–	–	–
B1	22 03 26.4	−03 41 35.5	–	–	–	–
B2	22 03 26.4	−03 42 15.5	–	–	–	–
B3	22 03 26.4	−03 42 55.5	–	–	–	–
B4	22 03 26.4	−03 43 35.5	–	–	–	–
B5	22 03 26.4	−03 44 15.5	–	–	–	–
B6	22 03 26.4	−03 44 55.5	–	–	–	–
B7	22 03 26.4	−03 45 35.5	–	–	–	–
B9	22 03 26.4	−03 46 55.5	–	–	–	–
B10	22 03 26.4	−03 47 15.5	–	–	–	–

[a] The table includes a summary of searches for other molecules in the directions. *Plus sign*: molecule has been detected; *minus sign*: molecule not yet searched for; *asterisk*: molecule searched for but not detected.

100–1000 pc. The comparisons of optical absorption and radio emission observations are complicated by the fact that part of the CO emission may come from material lying behind the star. Cases in which this confusion is obviously present were therefore excluded from the sample. For example, HD 37903 illuminates the dense reflection nebula NGC 2023 from the near side and shows rather weak foreground absorption.

The high-latitude positions were taken mostly from the survey of Magnani, Blitz, and Wouterloot (1988). In particular, positions were chosen for which CO $J = 1 \rightarrow 0$ line parameters are listed, and for which other molecules, such as OH and H_2CO, have been detected. A few places where C_3H_2 and H_2CO have been observed by Turner, Rickard, and Lan-ping (1989) have been added to the list. Finally, the line of sight toward HD 210121, a high-latitude star with strong interstellar CH, CH^+, C_2, and CN lines (de Vries and van Dishoeck 1988*a*, *b*, 1990) has been observed. The area surrounding HD 210121 has been mapped extensively in CO $J = 1$–0 by Gredel *et al.* (1990), and a few of their peak positions offset from the star were studied as well. Table 1 summarizes the observed positions and indicates in which directions optical absorption lines of C_2 or radio emission lines of OH, H_2CO, or C_3H_2 have been detected.

III. RESULTS

In Tables 2 and 3, the results of the observations obtained at the various telescopes are presented for the translucent and the high-latitude clouds, respectively. Table 4 lists the measured ^{13}CO intensities. Tables 5 and 6 summarize the results for the HD 210121 cloud. Where the line is resolved, both the peak antenna temperature T_A^*, the line width ΔV, and the integrated antenna temperature $\int T_A^* dV$ are listed. These parameters result from least-squares fits of Gaussian profiles to the lines. Some profiles show evidence of multiple components; the resulting Gaussians fitted to the profile are listed separately in Tables 2–6. However, as argued below (§ VI), alternative explanations for "double" profiles are possible in terms of effects of radiative transfer in inhomogeneous regions. For unresolved lines, only the integrated line strengths are tabulated. In cases where several components are observed to be separated by a few km s^{-1}, only those components which coincide in velocity with the optical absorption lines are listed. In some cases, the accuracy of the optical velocities is not high enough to make an unambiguous assignment. For example, the CO $J = 1 \rightarrow 0$ profile toward HD 80077 shows three components at $V_{LSR} =$ 2.1, 5.1, and 8.0 km s^{-1}. The optical absorption lines give $V_{LSR} = 2 \pm 2$ km s^{-1}. Although the agreement in velocity is best for the $V_{LSR} = 2.1$ km s^{-1} component, we cannot fully exclude the 5.1 km s^{-1} component. Figure 1 illustrates some of the $J = 2 \rightarrow 1$ and $3 \rightarrow 2$ profiles obtained at the CSO. In the following, we will comment on a few individual lines of sight.

CO $J = 1 \rightarrow 0$ and $2 \rightarrow 1$ line emission toward HD 21389 was observed by Lada and Blitz (1988). Their measured $T_R(2 \rightarrow 1) \approx 4.2$ K at the Texas 5 m Millimeter Wave Observatory (MWO) is somewhat higher than $T_R \approx 3.0$ K found at the CSO. In addition, the CSO profile clearly shows a double structure, which can be fitted with two components spaced 1 km s^{-1} apart. In contrast, the tabulated $1 \rightarrow 0$ linewidth of Lada and Blitz is much narrower than that of their $2 \rightarrow 1$ profile and appears to refer only to $V_{LSR} = -10.5$ km s^{-1} component. Accordingly, we have compared only the -10.5 km s^{-1} part of the $2 \rightarrow 1$ and $3 \rightarrow 2$ profiles with the $J = 1 \rightarrow 0$ data. For HD 21483, both the $1 \rightarrow 0$ and $2 \rightarrow 1$ profiles clearly have a double structure, as Figure 1 shows. However, in this case the decomposition into the two components is not unambiguous, so that only total line strengths are compared. The CO profiles toward HD 29647 exhibit a complicated velocity structure (cf. Fig. 1), which can be fitted by at least two Gaussians. The corresponding temperatures obtained for the $2 \rightarrow 1$ profile are nearly a factor of 2 lower than those measured by Crutcher (1985) at the MWO. For both HD 21389, HD 21483, HD 26571, and HD 29647, accurate velocity information on the optical absorption lines is lacking, so that it is not clear whether all components seen in CO are in front of the stars. The CO column densities derived from ultraviolet absorption line observations toward HD 26571 and HD 21483 are large, 10^{16}–10^{18} cm^{-2}, suggesting that most of the material does indeed lie in front of those stars (Joseph *et al.* 1986).

The velocities of the CO measured toward HD 62542, HD 73882, HD 147084 (*o* Sco), and HD 147889 agree well with those found from the absorption-line data. However, the measured CO antenna temperatures are much larger than expected on the basis of the extinctions toward these stars. It is therefore likely that part of the CO emission in these cases arises from material located behind the star. For HD 147889, for example, this is evidenced by a small reflection nebula. Since the fraction of material located in front of the star is not known, we have considered only the total intensities in the analysis. For the stars HD 154368, BD $-14°5037$, HD 169454, and HD 210072, it is plausible that most, if not all, emission at velocities of interest comes from CO located in front of the stars, so that direct comparison with the optical data is possible. For HD 154368, the $2 \rightarrow 1$ peak $T_R \approx 2.4$ K measured at SEST is lower than $T_R \approx 3.4$ K found at the MWO by Lada and Blitz (1988), although the integrated temperatures differ less. The HD 169454 cloud has been studied in detail by Jannuzi *et al.* (1988). The CO $2 \rightarrow 1$ temperature $T_R \approx 2.6$ K measured at the CSO is again somewhat lower than $T_R \approx 3.9$ K found by Lada and Blitz (1988) at the MWO. For BD $-14°5037$, two components spaced nearly 10 km s^{-1} apart were discovered in the optical absorption line data of Gredel and Münch (1986). Only the stronger component of the two at $V_{LSR} = 8.3$ km s^{-1} is seen in the millimeter data.

The "tiny" cloud α Ori No. 4 was discovered by Knapp and Bowers (1988). Based on their measured CO $1 \rightarrow 0/2 \rightarrow 1$ intensity ratios, they concluded that the cloud is highly clumped in the center. The fact that our measured CO $1 \rightarrow 0$ $T_R \approx 3.9$ K in the 44″ SEST beam is significantly larger than $T_R \approx 2.6$ K found with the 100″ Bell Labs beam, is consistent with this interpretation. The antenna temperature varies sharply in small-scale mapping at SEST with 25″ beam spacing. This structure must be considered in the comparison with the higher frequency transitions.

Most of the ^{12}CO and ^{13}CO $J = 1 \rightarrow 0$ line parameters for the high-latitude clouds are taken from Magnani, Blitz, and Wouterloot (1988). For lines measured at the MWO, an extended source efficiency of 0.8 was adopted to convert their measured T_A^* to T_R. At position MBM 54A, Blitz, Magnani, and Wandel (1988) have reported significant line "wings." These "wings" are also observed in our $2 \rightarrow 1$ and $3 \rightarrow 2$ profiles but do not appear more pronounced relative to the narrow peak than in the $1 \rightarrow 0$ data (see Falgarone and Phillips 1990 for an extended discussion of such line wings).

TABLE 2

CO OBSERVATIONS OF TRANSLUCENT CLOUDS

STAR	^{12}CO (1–0)					^{12}CO (2–1)					^{12}CO (3–2)				
	V_{LSR} (km s^{-1})	T_A^{*}[a] (K)	ΔV (km s^{-1})	$\int T_A^{*} dV$ (K km s^{-1})	Telescope[b]	V_{LSR} (km s^{-1})	T_A^{*}[a] (K)	ΔV (km s^{-1})	$\int T_A^{*} dV$ (K km s^{-1})	Telescope[b]	V_{LSR} (km s^{-1})	T_A^{*}[a] (K)	ΔV (km s^{-1})	$\int T_A^{*} dV$ (K km s^{-1})	Telescope[b]
HD 21389	−10.5	5.0	1.1	6.0	K[c]	−10.4	2.3	1.4	3.6	C/H	−10.6	1.3	0.7	1.0	C/H
	−9.4	...	...	...		−9.4	2.3	0.8	1.9	C/H	−9.5	2.0	0.8	1.7	C/H
	Total			6.0	K[c]	Total			5.4	C/H	Total			2.7	C/H
HD 21483	5.4	7.8	1.6	13.6	K	5.5	1.2	1.3	1.7[d]	C/H		...	...	...	
	7.1	3.6	2.1	8.1	K	6.6	2.7	3.0	8.7[d]	C/H		...	...	...	
	Total			21.3	K	Total			10.5	C/H	Total			6.6	C/L2
HD 26571	10.3	3.2	1.7	5.6	S	10.3	1.7	1.0	1.8	C/H		...	...	...	
		...	...	...		11.3	1.5	0.7	1.1	C/H		...	...	...	
	Total			5.6	S	Total			2.9	C/H	10.7	0.9	1.6	1.5	C/H
HD 29647	5.2	3.4	1.6	5.7	S	5.2	1.7	1.2	2.2	C/H	5.4	1.6	1.3	2.2	C/H
	7.1	2.4	2.2	5.6	S	7.1	1.2	2.6	3.3	C/H	6.8	0.8	1.6	1.3	C/H
	Total			11.3	S	Total			5.5	C/H	Total			3.5	C/H
α Ori 4	10.5	3.0	1.5	4.9	S[e]	10.3	3.7	1.6	6.5	K[e]	10.5	3.1	1.5	4.9	C/H
HD 62542	−4.2	7.8	1.5	12.8	S		...	...	...		−4.6	2.9	1.7	5.2	C/H
HD 73882	5.9	3.7	2.8	11.1	S[f]		...	...	...		5.4	0.9	2.6	2.6	C/H
HD 80077	2.1	1.0	1.9	2.1	S		...	...	≤0.4	C/L2	2.1	...	...	≤0.4	C/H
	5.1	3.6	1.1	4.1	S		...	...	4.7	C/L2	4.8	1.0	0.6	0.7	C/H
	Total	...	...	6.2	S[g]		...	...	4.7	C/L2		...	...	1.1	C/H
HD 147084	4.1	8.2	1.0	8.7	K		...	...	5.6	C/L2	4.0	2.1	1.1	2.4	C/H
HD 147889	2.9	10.2	2.0	22.1	S		...	...	14.0	C/L2	2.8	4.3	2.2	10.1	C/H
ζ Oph	−0.8	1.6	0.6	1.0	I	−0.8	0.8	0.6	0.5	I	−0.8	≤0.08	...	≤0.05	C/H
	0.4	0.7	0.9	0.6	I	0.4	0.3	1.1	0.3	I	0.4	≤0.08	...	≤0.08	C/H
	Total			1.7	I[h]	Total			0.8	I[h]	Total			≤0.13	C/H
HD 154368	5.0	2.6	0.7	1.8	S		...	...	...		...	...	...		
	5.8	3.2	1.0	3.6	S		...	...	...		...	...	...		
	Total			5.3	S[i]	5.6	1.8	1.9	3.7	S	5.4	0.7	1.7	1.3	C/H
BD −14°5037	8.3	3.6	1.0	4.0	K[j]		...	...	...		8.2	0.7	0.8	0.6	C/H
HD 169454		...	...	...		5.8	1.8	0.7	1.2	C/H		...	...	...	
		...	...	...		6.6	2.1	1.0	2.2	C/H		...	...	...	
	Total	4.7	1.3	6.5	K[k]	Total			3.4	C/H	6.0	1.2	1.2	1.4	C/H
HD 210072	−6.2	1.9	1.1	2.3	K		...	...	...			...	...	0.7	C/L1

[a] For data obtained at Kitt Peak, T_R^{*} rather than T_A^{*} is listed.

[b] K = Kitt Peak 12 m; S = SEST 15 m; C/H = CSO with high resolution AOS; C/L1 = CSO with low-resolution AOS 1988 July; C/L2 = CSO with low-resolution AOS 1989 March; T = Texas MWO 5 m; I = IRAM 30 m; B = AT&T Bell Labs 7 m.

[c] From Lada and Blitz 1988.

[d] Decomposition into two Gaussians is not unique.

[e] CO 2 → 1 data from Knapp and Bowers 1988, who found $T_A^{*}(1 \rightarrow 0) = 2.4$ K using the Bell Labs telescope.

[f] There are second and third components at $V_{LSR} = 9.7$ and 11.8 km s^{-1}, which are not included.

[g] There is a third component at $V_{LSR} = 8$ km s^{-1}, which is not included in the total.

[h] From Le Bourlot, Gérin, and Pérault 1989. The temperatures have been corrected already for spillover and coupling efficiency.

[i] The integrated line intensity measured at Kitt Peak is 6.6 K km s^{-1}.

[j] The integrated line intensity measured at SEST is 2.6 K km s^{-1}.

[k] The line profile measured at SEST can be decomposed into two components at $V_{LSR} = 5.8$ and 6.5 km s^{-1} with a total integrated line intensity of 4.8 K km s^{-1}.

1991ApJ...366..141V

TABLE 3

CO OBSERVATIONS OF HIGH-LATITUDE CLOUDS

	^{12}CO (1–0)					^{12}CO (2–1)					^{12}CO (3–2)				
CLOUD	V_{LSR} (km s^{-1})	T_A^*[a] (K)	ΔV (km s^{-1})	$\int T_A^* dV$ (K km s^{-1})	Telescope[b]	V_{LSR} (km s^{-1})	T_A^*[a] (K)	ΔV (km s^{-1})	$\int T_A^* dV$ (K km s^{-1})	Telescope[b]	V_{LSR} (km s^{-1})	T_A^*[a] (K)	ΔV (km s^{-1})	$\int T_A^* dV$ (K km s^{-1})	Telescope[b]
MBM 26A	0.2	2.7	1.0	2.8	T[c]		...	...	2.5	C/L2		...	...	≤0.7	C/L2
MBM 32A		...	...	...			...	...	5.5	C/L2		...	...	1.8	C/L2
MBM 32B		4.0	1.3	5.5	T[c]		...	...	3.7	C/L2		...	...	1.1	C/L2
MBM 32D	4.0	5.3	0.9	5.1	K[c]		...	...	5.6	C/L2		...	...	1.9	C/L2
MBM 40A	3.5	5.7	0.5	3.0	T[c]		...	...	...			...	...	...	
	4.1	1.2	0.9	1.2	T[c]		...	...	...			...	...	...	
	Total			4.2	T[c]		...	...	3.2	C/L2	3.0	1.0	1.2	1.3	C/H
MBM 40B	3.0	9.9	0.6	6.3	K[c]		...	...	5.6	C/L2	3.0	2.7	0.7	2.1	C/H
MBM 40C	3.9	4.7	1.0	5.0	T[c]		...	...	2.6	C/L2	3.4	0.9	1.4	1.3	C/H
MBM 40D							...	...	3.5	C/L2	2.8	1.1	0.9	1.1	C/H
MBM 53A	−3.7	3.6	1.1	4.2	K	−3.2	1.6	1.0	1.8	C/H	−3.3	0.6	0.7	0.5	C/H
MBM 54A	−3:	...	...	3.7	K	−2.6	2.2	1.0	2.4	C/H	−2.8	1.1	0.9	1.1	C/H
MBM 55A	−4.3	4.3	1.8	8.2	T[c]		...	...	...		−3.3	0.7	2.1	1.7	C/H
MBM 55B	−7.8	3.0	1.3	4.2	K[c]		...	...	...			...	...	...	
	−6.8	2.9	2.2	6.8	K[c]		...	...	...			...	...	...	
	Total			10.9	K[c]		...	...	...		−7.3	1.2	2.4	3.1	C/H
MBM 55D	−7.4	5.2	3.0	16.6	T[c]		...	...	...		−7.9:	1.7	2.6	4.4	C/H

[a] For data obtained at Kitt Peak, T_R^* rather than T_A^* is listed.

[b] K = Kitt Peak 12 m; C/H = CSO with high resolution AOS; C/L1 = CSO with low-resolution AOS 1988 July; C/L2 = CSO with low-resolution AOS 1989 March; T = Texas MWO 5 m.

[c] From Magnani, Blitz, and Wouterloot 1988.

TABLE 4

^{13}CO OBSERVATIONS OF TRANSLUCENT AND HIGH-LATITUDE CLOUDS

A. STARS

STAR	^{13}CO (1–0) V_{LSR} (km s^{-1})	T_A^* [a] (K)	ΔV (km s^{-1})	$\int T_A^* dV$ (K km s^{-1})	Telescope[b]
HD 21389	−10.5	0.7	0.7	0.5	K[c]
	−9.4	...	...	...	
	Total			0.5:	K[c]
HD 21483	5.4	2.2	1.3	3.0	K
	7.1	0.3	...	...	K
	Total			3.5	K
HD 26571	10.4	0.5	1.2	0.6	S
HD 29647	5.3	2.4	1.0	2.4	S
	6.7	1.4	1.2	1.7	S
	Total			4.1	S
α Ori No. 4	10.3	0.11	1.14	0.14	B[d]
HD 62542	−4.2	0.8	1.1	1.0	S
HD 73882	5.9	0.6	2.5	1.5	S
HD 80077	2.0	0.2	1.2	0.3	S
	5.0	0.7	1.0	0.7	S
	Total	...	...	1.0	S
HD 147084	4.1	0.4	0.6	0.3	K
HD 147889	2.9	1.5			S
ζ Oph	−0.8	...	...	...	
	0.4	...	...	...	
	Total	0.02	0.3	0.01	B[e]
HD 154368	5.7	0.4	0.6	0.2	S
	6.4	0.7	0.6	0.4	S
	Total			0.7	
BD −14°5037	8.7	0.4	0.7	0.3	S
HD 169454	6.3	1.2	0.8	1.0	K[f]
HD 210072	−6.2	0.2	0.5	0.1	K

B. CLOUDS

CLOUD	^{13}CO (1–0) V_{LSR} (km s^{-1})	T_A^* [a] (K)	ΔV (km s^{-1})	$\int T_A^* dV$ (K km s^{-1})	Telescope[b]
MBM 26A	0.2	...	...	...	
MBM 32A	...	...	...	...	
MBM 32B	...	...	...	...	
MBM 32D	...	...	...	...	
MBM 40A	3.5	...	...	...	
	4.1	...	...	...	
	Total	...	...	...	
MBM 40B	3.0	3.0	0.4	1.3	K[g]
MBM 40C	3.9	0.7	0.9	0.7	T[g]
MBM 40D		...	...	...	
MBM 53A	−3.7	0.4:	0.7	0.3:	K[f]
MBM 54A	−3:	...	...	0.7	K[f,h]
MBM 55A	−3.8	0.6	1.7	1.0	S
MBM 55B	−7.7	1.0	1.3	1.3	S
	−6.2	0.4	1.0	0.4	S
	Total			1.7	S
MBM 55D	−7.4	1.5	1.6	2.6	K[f,g]

[a] For data obtained at Kitt Peak, T_R^* rather than T_A^* is listed.
[b] K = Kitt Peak 12 m; S = SEST 15 m; T = Texas MWO 5m; B = AT&T Bell Labs 7 m.
[c] From Lada and Blitz 1988.
[d] From Knapp and Bowers 1988.
[e] From Langer, Glassgold, and Wilson 1987.
[f] Data obtained at SEST agree within 20%.
[g] From Magnani, Blitz, and Wouterloot 1988.
[h] From Blitz, Magnani, and Wandel 1988.

1991ApJ...366..141V

TABLE 5

CO OBSERVATIONS OF SELECTED POSITIONS IN THE HD 210121 CLOUD

	^{12}CO (1–0)					^{12}CO (2–1)					^{12}CO (3–2)				
POSITION	V_{LSR} (km s^{-1})	T_A^*[a] (K)	ΔV (km s^{-1})	$\int T_A^* dV$ (K km s^{-1})	Telescope[b]	V_{LSR} (km s^{-1})	T_A^*[a] (K)	ΔV (km s^{-1})	$\int T_A^* dV$ (K km s^{-1})	Telescope[b]	V_{LSR} (km s^{-1})	T_A^*[a] (K)	ΔV (km s^{-1})	$\int T_A^* dV$ (K km s^{-1})	Telescope[b]
HD 210121	−6.2	2.2	1.7	4.1	K	−5.52	0.70	1.92	1.45	C/H	−5.69	0.57	1.36	0.82	C/H
	−6.2	2.1	1.5	3.3	S										
A	−6.0	4.1	1.2	5.3	S	−6.05	3.22	1.14	3.91	C/H	−6.16	1.92	1.05	2.14	C/H
B = B8	−6.7	2.6	1.3	3.5	S	−6.64	2.34	1.29	3.20	C/H	−6.63	1.46	1.13	1.76	C/H
B1	−6.7	1.6	1.3	2.2	S	−6.61	0.89	1.57	1.49	C/H		≤0.3	...	≤0.5	C/H
B2		...	...	...		−6.10	0.80	0.56	0.48	C/H		...	...	...	
		...	...	...		−7.03	1.77	0.96	1.80	C/H		...	...	...	
	−6.7	1.8	1.4	2.7	S	Total			2.28	C/H		≤0.5	...	≤0.8	C/H
B3	−6.7	3.1	1.2	4.0	S	−6.88	2.08	1.21	2.68[c]	C/H		...	...	...	
B4	−6.7	4.1	1.3	5.7	S	−6.61	3.03	1.17	3.76	C/H	−6.54	1.46	0.93	1.45	C/H
B5	−6.7	3.9	1.3	5.5	S	−6.75	4.03	1.11	4.78	C/H	−6.70	2.24	0.94	2.23	C/H
B6	−6.7	3.9	1.2	5.0	S	−6.67	3.30	1.10	3.86	C/H		...	...	...	
B7	−6.8	4.4	1.1	5.2	S	−6.70	3.40	1.09	3.96	C/H		...	...	...	
B9	−6.6	1.7	1.0	1.8	S	−6.61	1.54	0.94	1.54	C/H	−6.3:	0.55:	1.0:	0.6:	C/H
B10	−6.5	1.0	1.4	1.4	S	−6.45	0.57	1.51	0.93	C/H		...	...	...	

[a] For data obtained at Kitt Peak, T_R^* rather than T_A^* is listed.

[b] K = Kitt Peak 12 m; S = SEST 15 m; C/H = CSO with high resolution AOS.

[c] Broad ($\Delta V \approx 4$ km s^{-1}) underlying component present in spectrum. Total integrated intensity including broad component = 3.16 K km s^{-1}.

TABLE 6

^{13}CO OBSERVATIONS OF SELECTED POSITIONS IN THE HD 210121 CLOUD

POSITION	^{13}CO (1–0)				
	V_{LSR} (km s^{-1})	T_A^*[a] (K)	ΔV (km s^{-1})	$\int T_A^* dV$ (K km s^{-1})	Telescope[b]
HD 210121	−5.9	0.1	1.7	0.2	S
A	−5.9	1.1	0.9	1.1	S
B = B8		<0.15	...	<0.2	S
B1		≤0.15	...	≤0.2	S
B2		<0.15	...	<0.2	S
B3	−6.7	0.3	1.5	0.5	S
B4	−6.5	0.5	0.8	0.4	S
B5	−6.5	0.5	0.7	0.4	S
B6	−6.5	0.6	1.0	0.6	S
B7	−6.5	0.6	0.7	0.4	S
B9		<0.15	...	<0.2	S
B10		<0.15	...	<0.2	S

[a] For data obtained at Kitt Peak, T_R^* rather than T_A^* is listed.
[b] S = SEST 15 m.

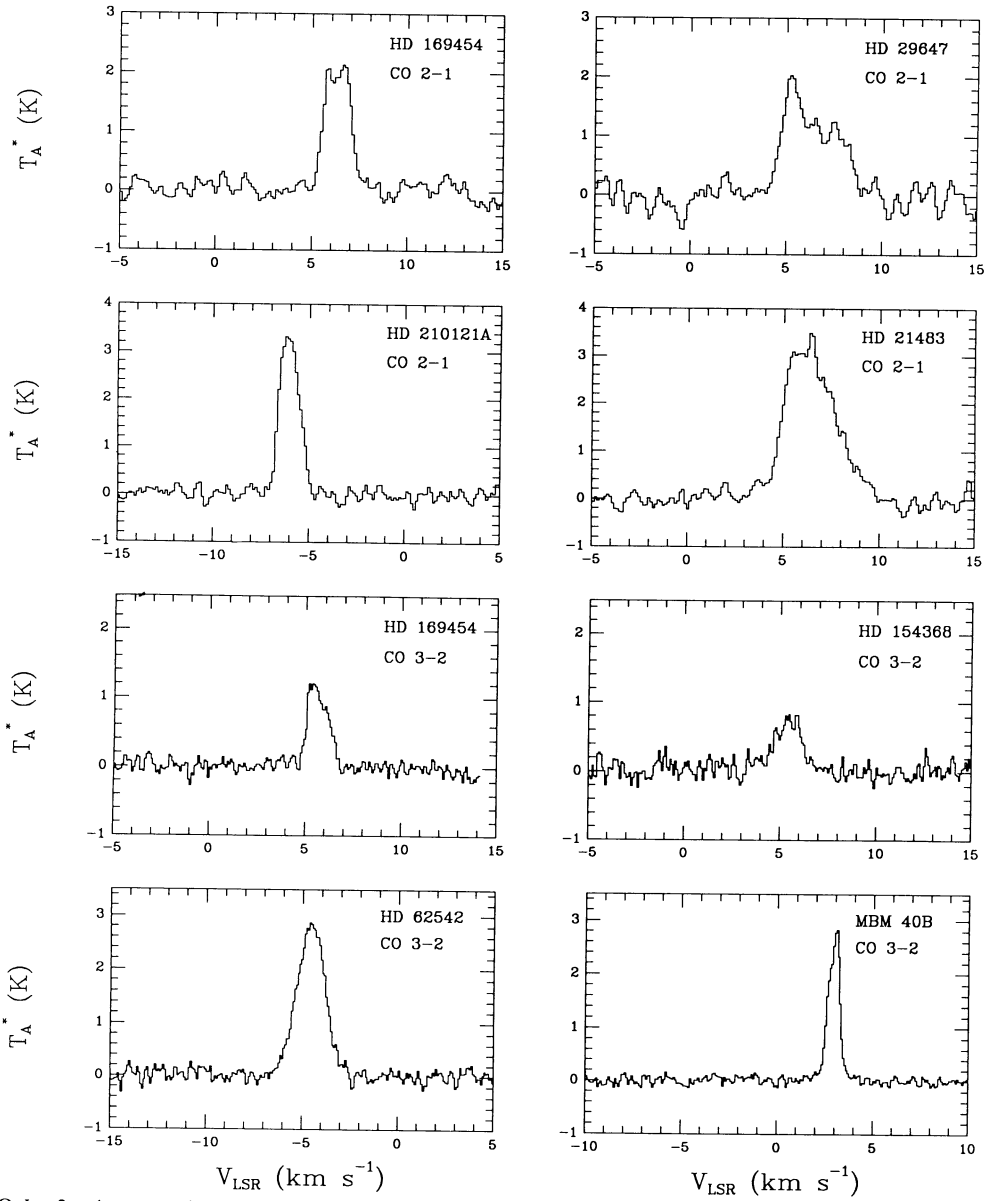

FIG. 1.—*Top half*: CO $J = 2 \rightarrow 1$ spectra obtained with the high-resolution AOS in 1989 October toward HD 169454, HD 210121A, HD 29647, and HD 21483. These spectra were taken under poor weather conditions, with total on-source integration times of 7.1, 5.8, 3.3, and 1.9 minutes, respectively. *Bottom half*: CO $J = 3 \rightarrow 2$ spectra obtained with the high-resolution AOS in 1990 March toward HD 169454, HD 154368, HD 62542 and MBM 40B under good weather conditions. Total on-source integration times are 10.5, 10.5, 10.5, and 7.9 minutes, respectively.

IV. ANALYSIS

a) ^{12}CO $J = 1 \rightarrow 0/3 \rightarrow 2$ *and* $J = 2 \rightarrow 1/3 \rightarrow 2$ *Intensity Ratios*

In Table 7, the integrated intensities corrected for cold spillover and coupling efficiencies are presented, together with the corresponding intensity ratios. For cases where the line is resolved, the ratios of peak radiation temperatures can be determined as well. Because the $1 \rightarrow 0$ lines are usually broader than the $3 \rightarrow 2$ lines, the ratios of peak temperatures are somewhat lower than the ratios of integrated temperatures, although the differences are generally within the uncertainties due to calibration.

CO excitation calculations have been performed for a range of densities, temperatures, and CO column densities. These calculations include the processes of spontaneous emission, stimulated emission and absorption in the 2.7 K cosmic background radiation field, and collisional excitation and deexcitation among the lowest 10 levels of the molecule. The radiative transfer is treated initially in terms of mean escape probabilities for an assumed uniform spherical cloud (see also § VI). The results are presented as T_R, the Rayleigh-Jeans approximation to the radiation temperature. For collisions of CO with H_2, the deexcitation cross sections of Schinke *et al.* (1985) at $T = 20$ K were adopted for low J and were augmented for higher J by those computed by Flower and Launay (1985). The uncertainties in the absolute cross sections are estimated to be about 20% and are probably less for the relative values. CO is also excited efficiently by collisions with H. If the cross sections computed by Chu and Dalgarno (1975) are adopted, the CO–H collisions increase the CO line strengths by 5%–30% for H_2/H ranging from 10 to 2. Because the actual fraction of H in the clouds is not well determined, we have not included CO–H collisions explicitly in our calculations but only implicitly by using an effective density of collision partners, $n = n(H) + n(H_2)$, which is the sum of atomic and molecular densities.

The clouds studied in this work are translucent to ultraviolet radiation, which can excite molecules as well as destroy them. The ultraviolet excitation can be shown to be negligible for CO. The CO absorption rate through the ultraviolet $A\ ^1\Pi$–$X\ ^1\Sigma^+$, $B\ ^1\Sigma^+$–$X\ ^1\Sigma^+$ and $C\ ^1\Sigma^+$–$X\ ^1\Sigma^+$ systems is about 8×10^{-10} s^{-1} in the unattenuated radiation field of Draine (1978); absorption into higher excited states leads to dissociation of the molecule. At the depth where the CO abun-

TABLE 7

CO INTEGRATED ANTENNA TEMPERATURE RATIOS

Position	$\int T_R dV$[a] 1–0	2–1	3–2	^{13}CO 1–0	1–0/3–2	2–1/3–2	3–2/^{13}CO 1–0	$N(CO)_{pr}$[b] (cm^{-2})	$N(CO)_{range}$[c] (cm^{-2})
HD 21389	6.0	4.6	1.4	0.5	4.4	3.5	2.7	1(16)	5(15)–3(16)
HD 21483	21.3	13.6	8.9	3.5	2.4	1.5	2.5	5(16)	1(16)–1(17)
HD 26571	6.8	3.8	2.0	0.7	3.4	1.9	2.9	2(16)	8(15)–4(16)
HD 29647	13.8	7.1	4.7	5.0	1.9	1.5	1.0	3(16)	8(15)–5(16)
α Ori 4	≥6.0	7.2	6.6	≥0.2	≥0.9	1.1	≤42	2(16)	6(15)–3(16)
HD 62542	15.6	...	7.0	1.2	2.2	...	5.8	2(16)	1(16)–1(17)
HD 73882	13.5	...	3.5	1.8	3.8	...	1.9	3(16)	1(16)–1(17)
HD 80077	7.6	6.1	1.5	1.2	5.1	4.0	1.3	1(16)	6(15)–3(16)
HD 147084	8.7	7.3	3.2	0.3	2.7	2.3	10.6	2(16)	1(16)–1(17)
HD 147889	27.0	18.2	13.6	2	2.0	1.3	6.8	5(16)	3(16)–4(17)
ζ Oph	1.7	0.8	≤0.2	0.01:	≥10.0	≥4.8	...	2(15)	1(15)–3(15)
HD 154368	6.5	4.9	1.8	0.9	3.7	2.8	1.9	1(16)	6(15)–3(16)
BD −14° 5037	4.0	...	0.8	0.5	4.9	...	1.6	6(15)	4(15)–2(16)
HD 169454	6.5	4.4	1.9	1.0	3.4	2.3	1.9	2(16)	5(15)–4(16)
HD 210072	2.3	...	1.0	0.1	2.3	...	10.0	4(15)	2(15)–6(15)
MBM 26A	3.5	3.2	≤0.9	...	≥3.9	≥3.5	...	5(15)	3(15)–1(16)
MBM 32A	...	7.1	2.4	...	...	3.0	...	2(16)	8(15)–5(16)
MBM 32B	6.9	4.8	1.5	...	4.6	3.2	...	2(16)	6(15)–5(16)
MBM 32D	5.1	7.3	2.6	...	2.0	2.8	...	2(16)	8(15)–5(16)
MBM 40A	5.3	4.2	1.8	...	3.0	2.4	...	2(16)	6(15)–5(16)
MBM 40B	6.3	7.3	2.8	1.3	2.2	2.6	2.1	3(16)	9(15)–9(16)
MBM 40C	6.3	3.4	1.8	0.9	3.6	1.9	1.9	2(16)	6(15)–5(16)
MBM 40D	...	4.5	1.5	...	...	3.0	...	2(16)	6(15)–5(16)
MBM 53A	4.2	2.3	0.7	0.3:	6.0	3.3	2.3	8(15)	4(15)–2(16)
MBM 54A	3.7	3.1	1.5	0.7	2.5	2.1	2.1	5(15)	4(15)–2(16)
MBM 55A	10.3	...	2.3	1.2	4.5	...	1.9	3(16)	1(16)–5(16)
MBM 55B	10.9	...	4.2	2.0	2.6	...	2.1	2(16)	8(15)–5(16)
MBM 55D	20.8	...	5.9	2.6	3.5	...	2.3	3(16)	2(16)–1(17)
HD 210121	4.1	1.9	1.1	0.2	3.7	1.7	5.5	7(15)	2(15)–1(16)
A	6.5	5.1	2.9	1.3	2.2	1.8	2.2	8(15)	6(15)–3(16)
B = B8	4.3	4.2	2.4	<0.3	1.8	1.8	>8	5(15)	4(15)–2(16)
B1	2.7	1.9	≤0.6	≤0.3	≥4.5	≥3.2	...	3(15)	2(15)–7(15)
B2	3.3	3.0	≤1.1	<0.3	≥3.0	≥2.7	...	4(15)	3(15)–8(15)
B4	6.9	4.9	2.0	0.5	3.5	2.5	4.0	7(15)	6(15)–4(16)
B5	6.7	6.2	3.0	0.5	2.2	2.1	6.0	7(15)	6(15)–4(16)
B9	2.2	2.0	0.8:	≤0.3	2.8	2.5	>2.7	3(15)	2(15)–6(15)

[a] Integrated antenna temperature ratios in K km s^{-1}, corrected for spillover and coupling efficiencies.
[b] Preferred column density based on best estimate of density.
[c] Range of column densities for $T = 20$–50 K and $n = 200$–5000 cm^{-3}.

dance is significant (i.e., detectable by its millimeter emission), the rate has decreased by a factor of at least 5. The pumping rate leading to population of the higher rotational levels is likely to be some fraction (about $\frac{1}{3}$–$\frac{2}{3}$) of this rate. Thus the CO ultraviolet pumping rate will be at most 10^{-10} s^{-1} in the general background starlight. For comparison, collisional excitation rate coefficients are typically 1×10^{-10} cm^3 s^{-1} at $T = 20$ K, so that for any density $n_H > 10$ cm^{-3}, the collisions easily dominate. Moreover, the rate of stimulated absorption in the 2.7 K background radiation field is 3.2×10^{-8} s^{-1} for the 1–0 transition, considerably larger than the pumping rate. Pumping through infrared vibration-rotation transitions is even less important in these regions. The absorption rate in $v = 1 \leftarrow 0$ is 1.0×10^{-11} s^{-1} in the background interstellar radiation field of Mathis, Mezger, and Panagia (1983).

In Figure 2 the computed $J = 1 \rightarrow 0/J = 3 \rightarrow 2$ and $J = 2 \rightarrow 1/J = 3 \rightarrow 2$ line ratios are presented for $T = 15$, 30, and 50 K, and densities $n = n(\mathrm{H}) + n(\mathrm{H_2})$ ranging from 200 to 5000 cm^{-3}. When CO column densities exceed 10^{15} cm^{-2}, the millimeter lines start to saturate, so that the line ratios vary with total column density. At very high densities and column densities, the excitation temperatures approach the thermal values. Because the excitation energy of the $J = 3$ level is 33.2 K, significant differences appear between the $T = 15$ and 30 K results. Table 7 includes the best estimates of the ^{12}CO column densities for the various lines of sight, obtained by

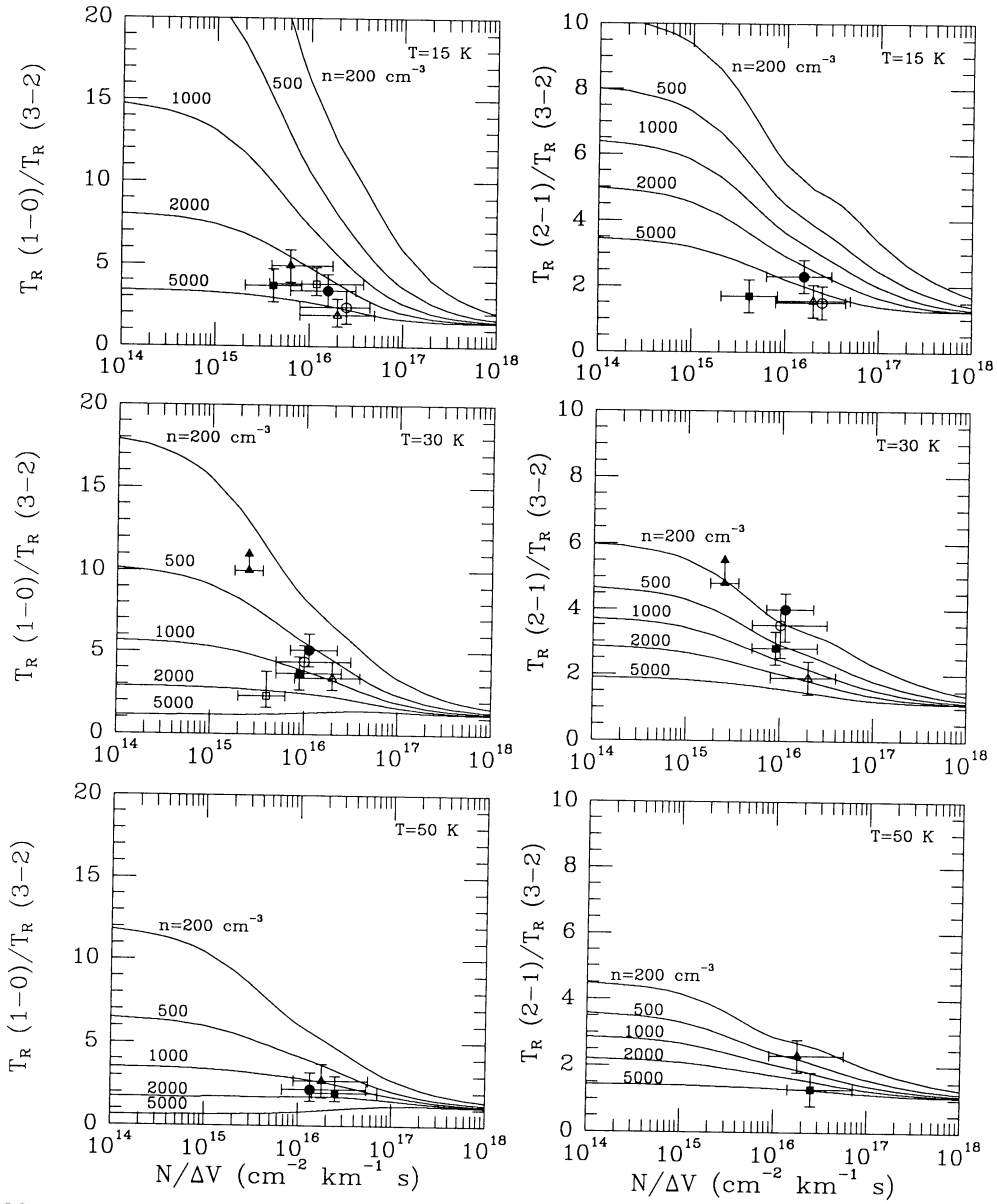

FIG. 2.—Theoretical CO antenna temperature ratios as functions of CO column density for $T = 15$ K (*top*), 30 K (*middle*), and 50 K (*bottom*) and densities n ranging from 200 to 5000 cm^{-3}. The observed ratios are indicated by the various symbols. *Top panels*: *open symbols*: *open circle*: HD 21483; *open triangle*: HD 29647; *open square*: HD 73882, *filled symbols*: *filled circle*: HD 169454; *filled triangle*: BD −14°5037; *filled square*: HD 210121. *Middle panels*: *open symbols*: *open circle*: HD 21389; *open triangle*: HD 26571; *open square*: HD 210072; *filled symbols*: *filled circle*: HD 80077; *filled triangle*: ζ Oph; *filled square*: HD 154368. *Bottom panels*: *filled symbols*: *filled circle*: HD 62542; *filled triangle*: HD 147084; *filled square*: HD 147889.

comparing the measured $J = 1 \rightarrow 0$ intensity with the models mentioned above. The large error bars reflect the full range of models, although in many cases they could be reduced considerably if restricted to the most likely range of densities based on the observed line ratios.

The observed $J = 1 \rightarrow 0/3 \rightarrow 2$ and $2 \rightarrow 1/3 \rightarrow 2$ ratios for the translucent clouds are included in Figure 2, whereas those for the high-latitude clouds are shown in Figure 3 for $T = 20$ K. The horizontal error bars indicate the full range permitted by the models, whereas the vertical error bars reflect the estimated uncertainties in calibration. In general, the observations for both sets of clouds are well bracketed by the range of densities $n = 200$–5000 cm^{-3}. No significant difference is found between the translucent and high-latitude clouds. For lower temperatures, the higher densities are favored, whereas for higher temperatures, the lower part of the density range is indicated. The $J = 2 \rightarrow 1/3 \rightarrow 2$ ratios indicate densities similar to those implied by the $J = 1 \rightarrow 0/3 \rightarrow 2$ ratios. This agreement suggests that the results are not very sensitive to the different beam sizes employed in the observations of the various lines.

i) *Translucent Clouds*

Better constraints on the densities can be obtained for individual translucent clouds in cases where information on the temperature is available from observations of the C_2 excitation. Consider as an example the line of sight toward HD 154368. The C_2 excitation in this cloud is well determined (van Dishoeck and de Zeeuw 1984) and indicates $T = 25 \pm 10$ K in the center of the cloud. CO is expected to be concentrated toward the center as well, although some models predict it to be more widely distributed throughout the cloud than C_2 (see § V). Since it is likely that such clouds have temperature gradients, the CO column-averaged temperature (see § V, eq. [2]) may be somewhat different from that of C_2, but probably not by more than 10 K. Accordingly, we have used $T = 20$–30 K in the analysis of the CO data for the HD 154368 cloud. For $T = 20$–30 K, both the observed $J = 1 \rightarrow 0/3 \rightarrow 2$ and $J = 2 \rightarrow 1/3 \rightarrow 2$ antenna temperature ratios can be reproduced with $n \approx 500$–2000 cm^{-3}, with a best value $n \approx 1000$ cm^{-3}. For comparison, the populations of the higher J levels of C_2 are compatible with $n\sigma_0/I_R \approx 5 \times 10^{-14}$ cm^{-1}. If the C_2 collisional cross section is taken to be $\sigma_0 \approx 2 \times 10^{-16}$ cm^2 and the scaling factor for the radiation field in the red $I_R \approx 1$, the resulting density is $n \approx 250$ cm^{-3}, somewhat below the density inferred from the CO observations, but close to the lower limit of the permitted range.

In Table 8 the temperatures and densities derived from the C_2 observations of translucent clouds are summarized and compared with the densities inferred from the CO observations. The results are not affected if the ratios of peak T_R rather than $\int T_R\, dV$ are considered. In all cases, the temperature in the CO analysis was allowed to be at most 10 K different from that indicated by the C_2 excitation. In the C_2 analysis, $\sigma_0 = 2 \times 10^{-16}$ cm^2 and $I_R = 1$ were adopted throughout. In general, the CO $J = 1 \rightarrow 0/3 \rightarrow 2$ ratios suggest densities that are higher than those derived from the C_2 excitation. For clouds like those toward HD 154368 and HD 80077, the discrepancy is only a factor of a few, which is not too serious in view of the uncertainties associated with both analyses. For the HD 62542, HD 73882, and HD 147889 clouds, the C_2 excitation provides only a lower limit to the density. Especially for HD 62542 and HD 147889, densities of at least 1000 cm^{-3} are implied by the C_2 high J populations. Both clouds appear to be warm, $T = 35$–55 K, which permits lower densities to be inferred from the CO antenna temperature ratios than would be the case at $T \approx 20$ K. For these clouds, the densities $n \approx 2000$–3000 cm^{-3} derived from CO are therefore not inconsistent with the C_2 analysis. In addition, Cardelli *et al.* (1990) have recently reported CN absorption line measurements toward HD 62542 that indicate a $\lambda = 2.6$ mm excitation temperature

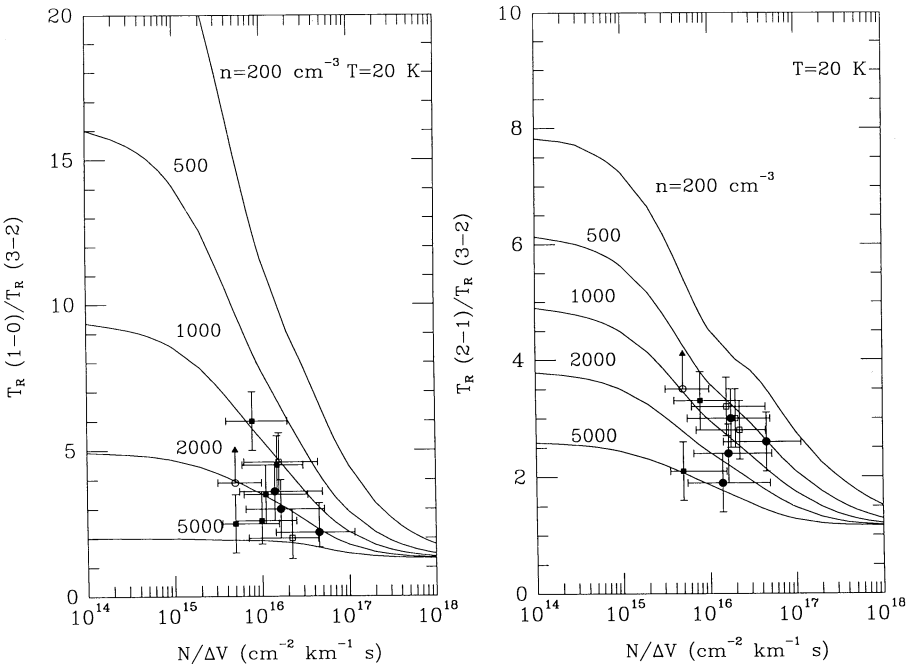

FIG. 3.—As in Fig. 2, but with the observed antenna temperature ratios for the high-latitude clouds. *Open symbols*: *open circle*: MBM 26; *open square*: MBM 32; *filled symbols*: *filled circle*: MBM 40; *filled square*: MBM 53–55.

TABLE 8

COMPARISON OF DENSITIES INFERRED FROM C_2 AND CO OBSERVATIONS

Position	C_2 Excitation			CO Excitation					
				1–0/3–2		2–1/3–2		3–2/^{13}CO 1–0	
	T (K)	n (cm^{-3})	Reference	n_{pr} [a]	n_{range} [b]	n_{pr}	n_{range}	n_{pr}	n_{range}
HD 21389	...	...	...	800	400–2000	500	200–2000	500	200–1000
HD 21483	...	...	...	3000	1000–5000	5000	2000–7000	800	300–1500
HD 26571	...	...	...	1000	500–2000	1500	700–5000	800	500–1500
HD 29647	15^{+10}_{-5}	350^{+300}_{-100}	1	4000	2000–7000	5000	2000–7000	500	200–1000
HD 62542	55 ± 10	≥300	2	1500	500–3000	...	...	1000	500–1500
HD 73882	20 ± 10	≥300	2	2000	1000–4000	...	...	1000	400–1500
HD 80077	25 ± 10	250 ± 100	3	700	400–1500	300	150–1000	200	100–300
HD 147084	40^{+10}_{-15}	200 ± 100	3	1000	500–2000	500	200–1500	1000	700–3000
HD 147889	55 ± 15	≥500	4	1500	500–3000	3000	1000–7000	1000	500–2000
ζ Oph	25 ± 10	150^{+100}_{-50}	5	≤200[c]	...	≤200[c]	...	...	...
HD 154368	25 ± 10	250^{+150}_{-100}	4	1000	500–2000	700	300–1500	300	200–500
BD −14° 5037	20 ± 10	250 ± 100	6	2000	1500–3000	...	...	600	200–1000
HD 169454	15^{+10}_{-5}	300^{+150}_{-100}	3, 6	2000	1500–4000	3000	1500–5000	600	200–1000
HD 210072	...	...	...	2000	1000–3000	...	...	1500	1000–3000
HD 210121	15^{+10}_{-5}	200^{+200}_{-100}	7	3000	1500–5000	6000	5000–8000	2000	1000–3000
MBM 26A	...	...	...	≤2000	...	≤1000	...	...	...
MBM 32A	...	...	...	...	...	700	300–1500	...	...
MBM 32B	...	...	...	1000	500–2000	700	400–1500	...	...
MBM 32D	...	...	...	3000	2000–5000	700	400–1500	...	...
MBM 40A	...	...	...	2000	1000–4000	1500	700–3000	...	...
MBM 40B	...	...	...	2000	1000–5000	700	300–2000	500	200–700
MBM 40C	...	...	...	1500	1000–3000	3000	1500–7000	300	200–500
MBM 40D	...	...	...	...	...	800	400–1500	...	...
MBM 53A	...	...	...	700	400–1500	700	300–1500	800	300–1000
MBM 54A	...	...	...	3000	1500–5000	4000	1500–6000	700	200–1000
MBM 55A	...	...	...	1000	500–2000	...	...	700	200–1000
MBM 55B	...	...	...	3000	1000–4000	...	...	700	200–1000
MBM 55D	...	...	...	2000	1000–3000	...	...	800	300–1000

[a] Preferred density in cm^{-3}.

[b] Range of densities permitted by errors in observations.

[c] See text for more detailed discussion.

REFERENCES.—(1) Hobbs, Black, and van Dishoeck 1983; (2) Gredel, van Dishoeck, and Black 1990; (3) van Dishoeck and Black 1989; (4) van Dishoeck and de Zeeuw 1984; (5) Danks and Lambert 1983; (6) Gredel and Münch 1986; (7) Gredel *et al.* 1990.

of $T_{ex} = 3.3 \pm 0.2$ K, which exceeds the brightness temperature of the cosmic background radiation. The excitation of CN requires an electron density $n(e) \approx 0.3$ cm^{-3} and thus implies densities $n(H_2) \approx 10^3$ to 4×10^3 for electron fractions $n(e)/n(H_2) \approx 10^{-4}$ to 10^{-5}, consistent with the CO and C_2 analyses (see Black and van Dishoeck 1990 for more details). The largest discrepancies occur for the HD 29647, HD 169454, and BD −14°5037 clouds, and for the high-latitude cloud HD 210121. These clouds are all thought to be cold, based on the C_2 data, so that $T \approx 15$ K has been adopted in the CO analysis. If the CO were located in a warmer part of the cloud ($T \approx 30$ K), the discrepancies would be reduced considerably. However, as argued in § V, this would require a rather special geometry and distribution. The discrepancy for HD 210121 is the largest and most puzzling. Admittedly, the C_2 absorption lines toward HD 210121 are only barely detected (Gredel *et al.* 1990), but the $J = 0/J = 2$ C_2 population ratio clearly indicates a low temperature, and the fact that the $Q(8)$ line is measurable suggests that the density is not much higher than 500 cm^{-3}. The differences could be explained if the cloud were highly clumped on scales of 20″ or less. Although the peak value of T_R is the same within 10% for measurements of CO $J = 1 \rightarrow 0$ made with antenna beam sizes between 40″ and 100″, a map of high signal-to-noise ratio obtained with SEST shows significant variations in line parameters on scales less than 60″. Note that the discrepancy is worse for the density derived from the $2 \rightarrow 1/3 \rightarrow 2$ ratio, even though the $2 \rightarrow 1$ data refer to a beam of only 32″.

Small-scale clumping definitely affects the analysis of the data for the α Ori No. 4 cloud, so that only lower limits on the $1 \rightarrow 0/3 \rightarrow 2$ and $2 \rightarrow 1/3 \rightarrow 2$ intensity ratios are possible in this case. These ratios suggest that the densities are no higher than 10^4 cm^{-3}, but do not constrain them further.

ii) *Diffuse Clouds: ζ Ophiuchi*

A sensitive search was made for the CO $J = 3 \rightarrow 2$ emission from the well-studied diffuse cloud toward ζ Oph. The CO $1 \rightarrow 0$ line profile in this direction is known to be complex, and can be decomposed into at least two narrow components at V_{LSR} −0.8 and +0.4 km s^{-1} with $T_R \approx 1.7$ and 0.7 K, and $\Delta V = 0.6$ and 0.9 km s^{-1}, respectively (Langer, Glassgold, and Wilson 1987; Le Bourlot, Gérin, and Pérault 1989). Similarly, the CO $2 \rightarrow 1$ profile consists of two narrow lines with $T_R \approx 0.8$ and 0.3 K, respectively (Crutcher and Federman 1987; Le Bourlot, Gérin, and Pérault 1989). However, the CO $J = 3 \rightarrow 2$ spectrum, presented in Figure 4, shows no apparent emission at these velocities. The formal 2 σ upper limit for each of the components is $T_A^* \approx 0.08$ K. Care has to be taken in the choice of the offset position for these measurements, since CO emission is very extended throughout the Ophiuchus cloud. We therefore obtained high signal-to-noise ratio spectra with both the offset position specified by Le Bourlot *et al.*, and by switch-

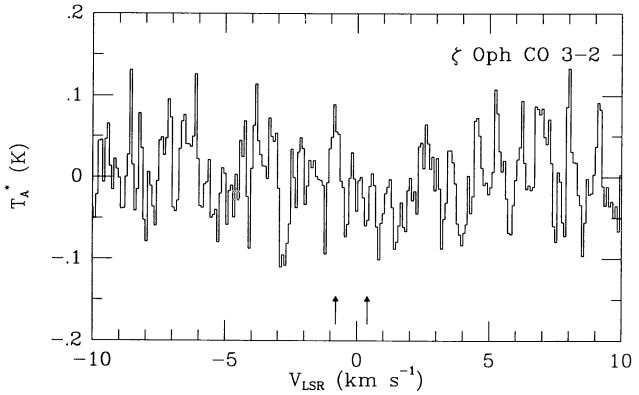

FIG. 4.—CO $J = 3 \rightarrow 2$ spectrum toward ζ Oph obtained with the high-resolution AOS in 1990 March. The total on-source integration time is 52 minutes. The arrows indicate the velocities of the observed CO $J = 1 \rightarrow 0$ and $2 \rightarrow 1$ lines.

ing in azimuth by $-60'$. Neither spectrum shows any feature at the level $T_A^* \approx 0.1$ K, so that failure to detect the $3 \rightarrow 2$ emission is unlikely to be due to accidental cancellation in the offset position. The spectrum presented in Figure 4 is the average of the spectra obtained with the two offset positions.

The low upper limit on the CO $3 \rightarrow 2$ emission can be used to place stringent limits on the density in the ζ Oph cloud, which has been subject to considerable discussion over the last 15 years. The original two-component model of Black and Dalgarno (1977) had a fairly high density, $n_H = n(H) + 2n(H_2) = 2500$ cm^{-3} in the center of the cloud, but subsequent analyses (Crutcher and Watson 1981; van Dishoeck and Black 1986*a*) suggested much lower densities, $n_H \approx$ 200–800 cm^{-3}. In particular, the C_2 rotational excitation indicates a low central density, $n_H \approx 250$ cm^{-3}, and a low central temperature, $T \approx 25$ K (van Dishoeck and Black 1986*b*). On the other hand, Viala, Roueff, and Abgrall (1988) have developed models of the ζ Oph cloud which retain a high central density, $n_H \approx$ 1000–5000 cm^{-3}. The CO $J = 3 \rightarrow 2$ observations can discriminate between these models: In the preferred model G of van Dishoeck and Black (1986*a*) the $3 \rightarrow 2$ line strength is predicted to be $T_R = 0.05$ K, whereas in model 6 of Viala, Roueff, and Abgrall (1988) it is $T_R = 0.57$ K (see van Dishoeck and Black 1988*a*, Table 4). These estimates include explicitly the excitation of CO by atomic hydrogen, which is significant in this cloud. The measured 2 σ upper limit, $T_R \leq$ 0.11 K, excludes the high-density models of Viala *et al.* and is only barely consistent with model G of van Dishoeck and Black. If the CO column-averaged temperature (see eq. [2], § V) is as low as 25 K and if $n(H) \approx 0.5n(H_2)$ on average, the CO $3 \rightarrow 2$ limit implies $n(H_2) \leq 200$ cm^{-3}, corresponding to $n_H \leq 500$ cm^{-3} for the strongest component. For the weaker component at $V_{LSR} = 0.4$ km s^{-1}, the limits are less stringent: $n(H_2) \leq 700$ cm^{-3}, corresponding to $n_H \leq 1750$ cm^{-3}. Since CO is thought to be formed in diffuse clouds mostly from the reaction of C^+ with OH and since OH is predominantly formed in the warmer, outer part of the cloud, the CO column-averaged temperature may be somewhat higher than the central temperature, $T(CO) \approx 40$ K. At $T = 40$ K, the CO $3 \rightarrow 2$ limit implies $n(H_2) \leq 150$ cm^{-3}, corresponding to $n_H \leq$ 425 cm^{-3} for the main component, and $n(H_2) \leq 500$ cm^{-3}, corresponding to $n_H \leq 1250$ cm^{-3} for the weaker component. Because the optical depth in the ^{12}CO $J = 1 \rightarrow 0$ line is low, $\tau \approx$ 1–2, these results are not affected if a more complicated radiative transfer method is employed (see also § VI). As will be discussed in more detail by Black and van Dishoeck (1990), the observed CN excitation by Crane *et al.* (1989) toward ζ Oph also indicates a low density, $n_H \leq 700$ cm^{-3}, for the main component.

In summary, the failure to detect the CO $J = 3 \rightarrow 2$ line at the level $T_R \approx 0.11$ K for the main component of the ζ Oph cloud is consistent with the analysis of the C_2 excitation, which suggests $n_H \approx 250$ cm^{-3} in the region where these molecules exist. It also indicates that the two methods give densities which differ at most a factor of 2, at least for this low-density, low column density cloud.

iii) *High-Latitude Clouds*

No comparisons with densities derived from the C_2 excitation are possible for the observed positions in the high-latitude clouds of Magnani, Blitz, and Wouterloot (1988). The densities derived from the CO line ratios in these clouds are not significantly different from those found for the translucent clouds. Cloud MBM 40 may be the densest at some locations, although this may result partly from small-scale clumping, which leads to an underestimate of the $1 \rightarrow 0$ antenna temperature in the larger beam. The data for all the clouds appear to follow reasonably well the theoretical curves for $n =$ 1000–2000 cm^{-3} at $T = 20$ K. Turner, Rickard and Lan-ping (1989) have derived upper limits on the densities of 10^5 cm^{-3} in clouds MBM 26, 32, and 40 from measured H_2CO line ratios. These upper limits are consistent with the densities derived from CO, although their average densities of a few $\times 10^4$ cm^{-3} at other high-latitude positions are much higher than the densities of about 1000 cm^{-3} suggested by the CO line ratios. In particular, at position MBM 55D, Turner *et al.* derive $n \approx$ (3–8) $\times 10^4$ cm^{-3} compared with $n \approx 1000$ cm^{-3} found in this work. However, Turner *et al.* did not take the possibility of collisions with electrons into account. Inclusion of electron impact in the treatment of H_2CO excitation will make the inferred abundances and densities very sensitive to the electron fraction, $x(e) = n(e)/n(H_2)$, and will modify the conclusions of Turner *et al.* if the high-latitude clouds support values of $x(e)$ as large as 10^{-6}. According to model calculations (van Dishoeck and Black 1989), the electron fractions are expected to be of order 10^{-5} in these clouds. A recent reinvestigation of the excitation of H_2CO incorporates neutral impact, electron impact, ortho/para interchange, and processes of formation and destruction (Black and van Dishoeck 1991). Results of these calculations suggest that the 6 cm and 2 cm absorption line data summarized by Turner *et al.* are consistent with densities $n(H_2) \leq 10^4$ cm^{-3} for most of the MBM clouds when $x(e) \approx 5 \times 10^{-6}$ to 10^{-5}. The derived column densities of H_2CO lie in the range 10^{13}–10^{14} cm^{-2} for these clouds. This indicates that the abundances of H_2CO may not be low compared with those in low-latitude dark clouds as claimed by Turner *et al.* Drdla, Knapp, and van Dishoeck (1989) have previously shown that electron impact excitation is effective in making CS lines detectable in diffuse and translucent clouds of modest density.

b) ^{12}CO $J = 3 \rightarrow 2/^{13}$CO $J = 1 \rightarrow 0$ *Intensity Ratio*

Another method to derive densities from the CO observations is to consider the strength of the ^{12}CO $J = 3 \rightarrow 2$ line relative to that of the ^{13}CO $J = 1 \rightarrow 0$ line. When the ^{12}CO $J = 1 \rightarrow 0$ line is saturated, the comparison with the ^{13}CO line, which has about the same strength as the ^{12}CO $J = 3 \rightarrow 2$ line,

may be more revealing. Unfortunately, the analysis requires knowledge of the $^{12}CO/^{13}CO$ column density ratio. Although this ratio is close to the overall $[^{12}C]/[^{13}C]$ ratio in dense clouds, it can be affected in translucent clouds by isotope-selective photodissociation and low-temperature carbon isotope exchange reactions. Detailed cloud models (van Dishoeck and Black 1988*b*) indicate that the two effects tend to cancel each other, except at low temperatures $T \leq 20$ K, where the $^{12}CO/^{13}CO$ ratio may be lowered relative to $[^{12}C]/[^{13}C]$ by a factor of 2–3. The $[^{12}C]/[^{13}C]$ ratio in the local interstellar medium is currently subject to discussion: the recent literature yields values ranging from 45 to 75 (Hawkins and Jura 1987; Stahl *et al.* 1989). Accordingly, we have performed model calculations for $^{12}CO/^{13}CO$ varying between 20 and 50. Our observed ^{13}CO line strengths indicate $^{12}CO/^{13}CO$ ranging from 15 to 60 in the various clouds, although the measured ratios are very uncertain, owing to uncertainties in the ^{12}CO column densities.

Table 7 presents the observed ^{12}CO $J = 3 \rightarrow 2/^{13}CO$ $J = 1 \rightarrow 0$ integrated antenna temperature ratios. In general, the ^{13}CO line is even narrower than the ^{12}CO $J = 3 \rightarrow 2$ line, so that the ratios are lowered if peak temperatures rather than integrated temperatures are considered. ^{13}CO excitation calculations were performed in the manner described for ^{12}CO, but with the appropriate line frequencies and transition probabilities. The resulting intensity ratios for $T = 20$–30 K and for various ^{13}CO abundances are presented in Figure 5 as functions of density. Since both lines have small optical depths over the range of observed line strengths, the ratios do not vary significantly with column density. Optical depth effects tend to lower the model results only at the highest densities. Higher temperatures and higher $^{12}CO/^{13}CO$ abundance ratios tend to lower the inferred densities.

Figure 5 displays the observed line strength ratios for a number of clouds. For most cases, the observed ratios are about 1–2, suggesting rather low densities $n = 500$–1000 cm^{-3}, even for $^{12}CO/^{13}CO$ as low as 20. Only for the clouds HD 62542, HD 147084, HD 147889, HD 210121, and possibly HD 210072 are the ratios significantly larger. For HD 62542, HD 147084, and HD 147889, the higher temperature and the consequently larger $^{12}CO/^{13}CO$ ratio lead to densities $n \approx 1000$ cm^{-3} that are only slightly larger than those found for other clouds.

The densities consistent with the ^{12}CO $3 \rightarrow 2/^{13}CO$ $1 \rightarrow 0$

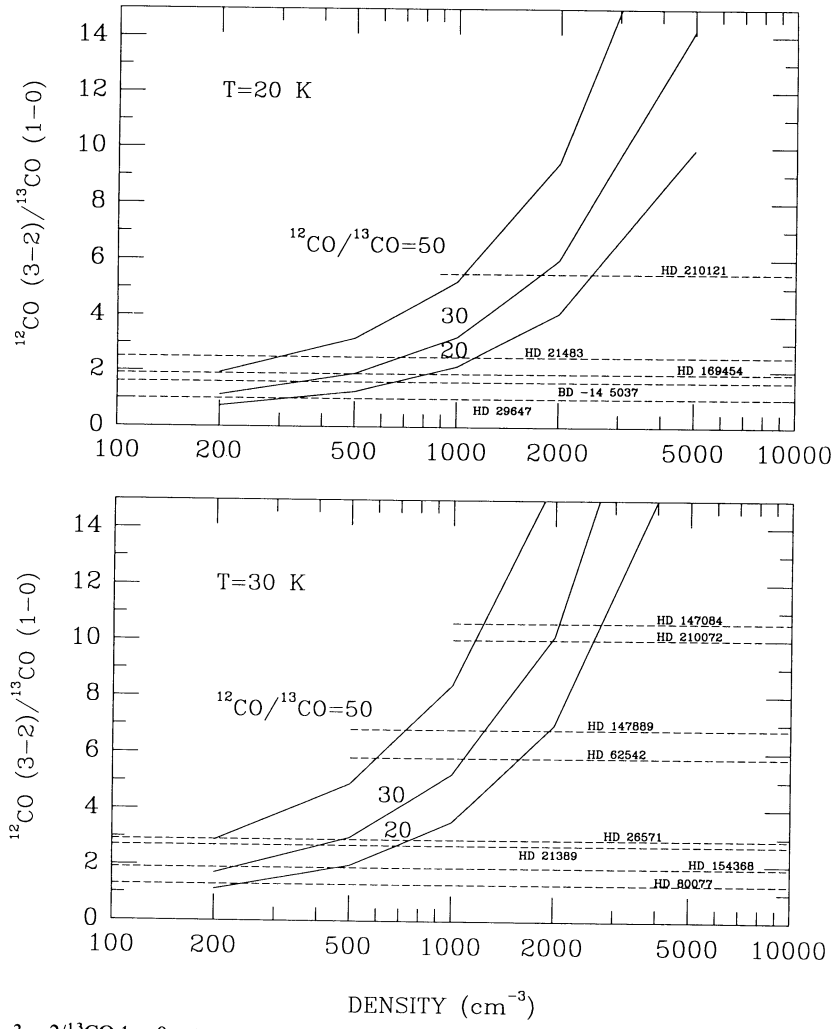

FIG. 5.—Theoretical ^{12}CO $J = 3 \rightarrow 2/^{13}CO$ $1 \rightarrow 0$ antenna temperature ratios as functions of density for $^{12}CO/^{13}CO$ column density ratios of 20, 30, and 50. The observed ratios for the various translucent clouds are indicated by the dashed lines. Intersection of the dashed and full lines gives the range of densities.

ratios are listed in Table 8. It is seen that these densities are generally lower than those inferred from the ^{12}CO $1 \rightarrow 0/3 \rightarrow 2$ or $2 \rightarrow 1/3 \rightarrow 2$ ratios, although the trend is the same. On the other hand, they agree within a factor of 2 with the densities inferred from the C_2 excitation, even for cold clouds such as HD 169454. The one exception is again the HD 210121 cloud: the ^{12}CO $3 \rightarrow 2/^{13}$CO $1 \rightarrow 0$ ratio indicates $n \approx 1000$–3000 cm^{-3}, significantly larger than $n \approx 200$ cm^{-3} derived from the C_2 data. For the high-latitude positions, the $3 \rightarrow 2/^{13}$CO $1 \rightarrow 0$ ratio also indicates relatively low densities, even for MBM 40 and MBM 54A.

c) *Discussion*

It thus appears that the ^{12}CO line intensity ratios imply densities that are up to an order of magnitude higher than those found from the observed C_2 excitation, whereas the ^{12}CO $3 \rightarrow 2/^{13}$CO $1 \rightarrow 0$ intensity ratio gives densities that differ by at most a factor of 2. Part of the discrepancy could arise from uncertainties in the parameters entering the C_2 analysis. The ratio σ_0/I_R was calibrated for the ζ Per diffuse cloud through comparison with other diagnostics (van Dishoeck and Black 1982). If the C_2 collisional cross section σ_0 were smaller by a factor of 2–3, the C_2 densities could be increased. Note, however, that this would also imply higher densities for the ζ Per cloud, in conflict with other diagnostics. Alternatively, the strength of the radiation field at $\lambda \approx 1$ μm could be higher than the value 8×10^5 photons s^{-1} cm^{-2} Å^{-1} adopted in this work for $I_R = 1$. According to Mathis, Mezger, and Panagia (1983), the standard interstellar radiation field at $\lambda \approx 1$ μm is 6×10^5 photons s^{-1} cm^{-2} Å^{-1}. If $I_R > 1$ for most of the observed clouds but not for the ζ Per cloud, the densities derived from the C_2 data could be increased as well. However, even bright reflection nebulae have surface brightnesses only 5 times higher than that of the interstellar radiation field at $\lambda \approx 1$ μm (cf. Sellgren, Werner, and Dinerstein 1983), so that isolated translucent clouds are unlikely to suffer greatly enhanced rates of C_2 pumping. In addition, the upper limit on the density in the ζ Oph cloud derived from the CO $J = 3 \rightarrow 2$ limit differs by at most a factor of 2 from that inferred from the C_2 excitation, suggesting that the parameters entering the C_2 analysis cannot be in error by more than a factor of 2.

An alternative explanation could lie in the small-scale structure of the clouds in several ways. The 44″–60″ antenna beams used in the $J = 1 \rightarrow 0$ measurements might couple to the emitting gas differently than the 20″ beam of the $J = 3 \rightarrow 2$ observations. This would cause $T_R(1 \rightarrow 0)$ to be underestimated from the measured $T_A^*(1 \rightarrow 0)$, with the result that the adopted value of $T_R(1 \rightarrow 0)/T_R(3 \rightarrow 2)$ would imply an overly high density. On the other hand, the $J = 2 \rightarrow 1$ data were obtained with a 32″ beam and the $T_R(2 \rightarrow 1)/T_R(3 \rightarrow 2)$ ratios suggest even larger densities in some cases. Internal structure can complicate the analysis in another way. If the clouds typically have gradients of density and temperature along the line of sight, then effects of radiative transfer through an inhomogeneous emitting region would allow different mean densities to be derived from those indicated for uniform clouds. We investigate this problem with respect to line profile shapes in § VI. Part of the discrepancy may also be due to the difference in angular scale of the emission and absorption line observations. The CO emission line data provide information on the physical properties averaged over a 20″–60″ beam, whereas the C_2 absorption samples a region with a size corresponding to the angular diameter of the background star, which is usually less than 0.″001. If the clouds are clumped on very small scales, it is possible that there exist regions of very high density that dominate the CO emission but which do not happen to lie along the line of sight to the star. In that case, the difference in densities derived from the CO and C_2 should provide constraints on the angular scale and the amplitude of the density fluctuations.

Another possibility, to be discussed further in § V, is that the CO and C_2 molecules are distributed differently throughout the cloud. As mentioned before, the largest discrepancies occur for clouds with the lowest temperatures derived from the C_2 excitation. If CO were located principally in a warmer region, the discrepancy would be reduced considerably.

Although these arguments may solve some of the discrepancy between the ^{12}CO and C_2 analyses, they cannot explain the difference between the ^{12}CO and ^{13}CO results. Part of this difference may arise from the fact that the ^{12}CO lines are slightly optically thick, $\tau \approx 1$–4 in most cases, whereas the ^{13}CO lines are optically thin, so that different parts of the cloud are sampled. The difference, then, would reflect the inadequacy of simple models of radiative transfer. This possibility will be further discussed in §§ V and VI. Alternatively, the ^{12}CO/^{13}CO ratio may be different from the range 20–50 considered here.

d) *Variation in Intensity Ratios across the HD 210121 Cloud*

Although for most clouds only a single position was observed in CO $J = 3 \rightarrow 2$, a small portion of the HD 210121 cloud was mapped. The strip in declination around position *B* at $(\Delta\alpha, \Delta\delta) = (-32.''5, 0')$ offset from the star was chosen because it shows significant variation in the $J = 1 \rightarrow 0$ emission on small scales (Gredel *et al.* 1990). The positions B1–B10 cover nearly 6′ ($\sim$0.26 pc at the estimated distance of the cloud of 150 pc) in steps of 40″ (0.029 pc). The observed $J = 2 \rightarrow 1$ antenna temperature variation is presented in Figure 6, together with the measured line temperature ratios. It appears that there is a suggestion of variation in both the $J = 1 \rightarrow 0/3 \rightarrow 2$ and $2 \rightarrow 1/3 \rightarrow 2$ ratios from the edge to the center of the cloud: the densities at the edge of the cloud would then be lower than those found at the center. The ^{12}CO $3 \rightarrow 2/^{13}$CO $1 \rightarrow 0$ ratios show a similar trend: the ratio is relatively low, about 3, at the edge and increases to more than 8 in the center.

If all physical parameters except density remained the same across the cloud, the observed variations in line intensity ratios would indicate a gradient in density from 1000–2000 cm^{-3} at the edge to 5000 cm^{-3} in the center. Since the temperature is likely to be higher at the edge due to increased heating by the photoelectric effect, the densities at the edge may be even lower, about 500–1000 cm^{-3}. Note that the minima in the intensity ratios, which presumably correspond to the maxima in density, do not appear to coincide with the maximum in the absolute intensity or column density. Indeed, the edge of the cloud to the south of position B appears to have a particularly steep decrease in both column density and density.

The $J = 2 \rightarrow 1$ intensity and the line ratios to the north of position B shown in Figure 6 can be fit well by a model that has a density distribution with radial distance R in pc of $n = 6000(1 - R/0.167)^{1.1}$ cm^{-3}, when the radiative transfer is treated in the Sobolev approximation. The mean density in this model is 2900 cm^{-3} and the inferred column density of CO through the peak position is $N(\mathrm{CO}) = 6 \times 10^{15}$ cm^{-2}. The inferred temperature is $T = 18$ K. The model requires ^{12}CO/^{13}CO = 16 to reproduce the ^{13}CO $J = 1 \rightarrow 0$ line intensity at the peak position. Consideration of gradients in the CO abun-

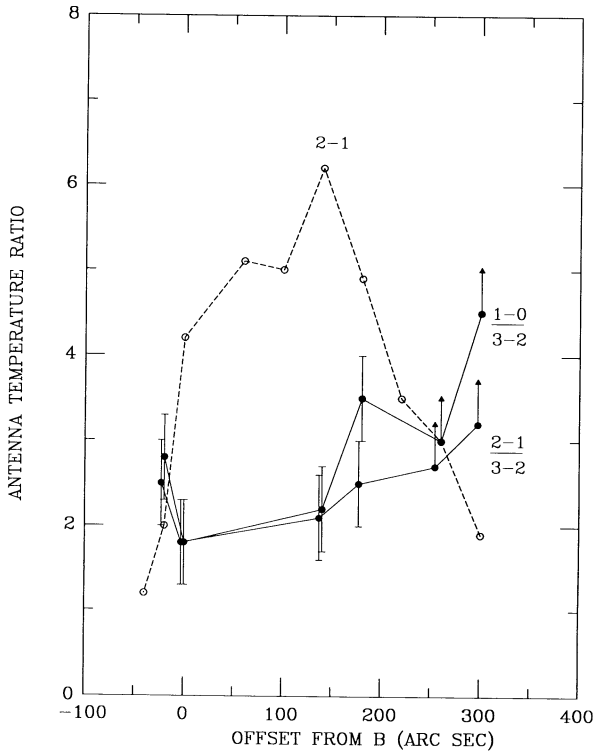

FIG. 6.—Variation of the ^{12}CO 1 → 0/3 → 2 and 2 → 1/3 → 2 antenna temperature ratios across a strip in declination around position HD 210121B. The dashed line indicates the variation in CO $J = 2 \rightarrow 1$ integrated radiation temperature, $\int T_R\, dV$, in units of K km s^{-1}.

dance and in temperature would permit the inferred density to be lower.

V. "CLUMPY" CLOUD MODELS

If the densities derived from the CO observations are indeed significantly larger than those inferred from the C_2 excitation, the question arises whether the CO and C_2 molecules are distributed differently throughout the cloud, or whether the emission-line observations sample material with different physical characteristics than the absorption-line observations, or both.

The distribution of CO and C_2 has been investigated in a number of homogeneous and inhomogeneous models, in which the concentrations are computed as functions of depth into the cloud. These distributions can be characterized conveniently by the weighted, column-averaged densities and temperatures, where

$$\langle \mathrm{H_2} \rangle_X = \int n(\mathrm{X}) n(\mathrm{H_2}) dz \Big/ \int n(\mathrm{X}) dz \,, \quad (1)$$

$$\langle T \rangle_X = \int n(\mathrm{X}) T\, dz \Big/ \int n(\mathrm{X}) dz \,, \quad (2)$$

and n(X) is the concentration of species X at depth z into the cloud. Table 9 lists the column-averaged properties for various molecules in the ζ Oph diffuse cloud model G (van Dishoeck and Black 1986*a*), and the translucent cloud models T3 and T4 (van Dishoeck and Black 1988*b*, 1989), which have temperatures varying from 80–100 K at the edge to 15–20 K in the center, and densities $n_H = n(H) + 2n(H_2)$ ranging between 200–300 cm^{-3} at the edge to 500–700 cm^{-3} in the center. Since

TABLE 9

COLUMN-AVERAGED DENSITIES AND TEMPERATURES

	CO		C_2			
MODEL[a]	$\langle T \rangle$[b]	$\langle H_2 \rangle$[c]	$\langle T \rangle$	$\langle H_2 \rangle$	CH $\langle H_2 \rangle$	CN $\langle H_2 \rangle$
ζ Oph G	49	120	47	125	120	125
T3	25	240	31	225	215	230
T4	25	325	40	275	280	300
S1	17	2660	17	2420	2210	2680
S2	16	2765	20	1915	1855	2345
S3	16	2790	25	1165	1370	1645
S4	16	2645	28	840	950	1170
S5	36	1225	18	2205	1940	2415
S6	37	1040	19	2110	1960	2385
S7	36	1285	23	1370	1565	1885
S8	35	1460	28	825	985	1140

[a] See text for description of the models.
[b] In K; see eq. (2) for definition.
[c] In cm^{-3}; see eq. (1) for definition.

the density contrast in the latter models is not very large, we also constructed a new set of models, denoted as S1–S8, in which the density n_H varies in discrete steps from 200 to 6000 cm^{-3} from edge to center, and the temperature from 80 to 15 K. About 55% of the size of these clouds is taken to be at $n_H = 200$ cm^{-3} and $T = 80$ K, about 30% at $n_H = 600$ cm^{-3} and $T = 50$ K, about 10% at $n_H = 2000$ cm^{-3} and $T = 25$ K, and about 4% at $n_H = 6000$ cm^{-3} and $T = 15$ K. Thus, the various layers have approximately equal masses. Models S1–S4 with $A_V^{tot} = 1$–3 mag are symmetric around the center and have the standard radiation field (cf. Draine 1978) incident on both sides of the cloud, whereas models S5–S8 have the radiation incident on one side only, but with otherwise the same physical parameters as S1–S4.

It appears from Table 9 that in diffuse clouds such as the ζ Oph cloud, CO is more widely distributed than C_2, leading to slightly higher column-averaged temperatures and slightly lower column-averaged densities. This results mostly from the fact that the concentration of OH, the principal precursor of CO, does not peak near the center of the cloud, but at intermediate depths where the higher temperature favors its formation (cf. Fig. 3 of van Dishoeck and Black 1986*a*).

However, in the translucent cloud models T3 and T4, and in the two-sided models S1–S4, CO is clearly more concentrated toward the colder and denser parts of the cloud than C_2. This difference in column-averaged temperature and density increases with larger total column density of the cloud. The lower density for C_2 results from the fact that in the densest parts of the cloud where $n_H = 6000$ cm^{-3}, the C^+ abundance is significantly reduced due to the enhanced carbon recombination rate. Since C_2 is mostly formed through reactions of C^+ with CH and CH_2, the C_2 abundance drops accordingly. For models of larger total column density, the reduced photoionization rate of C reduces the C^+ and C_2 abundances in the center even further. The CO abundance continues to increase toward the center of the cloud until all gas-phase carbon has been converted into CO. For model S4 with $A_V^{tot} = 3$ mag, this limiting abundance of CO is reached already at a depth where the density $n_H = 2000$ cm^{-3} rather than 6000 cm^{-3}, so that the CO column-averaged density is somewhat lower in this model compared with model S3.

If the models have the radiation incident from one side only, the situation is reversed: the C_2 column-averaged densities are

much larger, and the temperatures lower. This is easily explained by the fact that once the CO column density is large enough for the ultraviolet lines to become self-shielding, the CO photodissociation rate drops considerably and stays low throughout the rest of the cloud. Thus, the CO abundance stays large in the regions of low density on the far side of the cloud which is not exposed to radiation, resulting in lower column-averaged densities. The C_2 abundance is more concentrated toward the center, because the C^+ abundance is smaller on the far side of the cloud where the photoionization rate is reduced. The removal of C_2 itself is no longer dominated by photodissociation, but by reactions with O at those depths. The difference between CO- and C_2-averaged densities decreases for clouds of larger total column densities, because the C photoionization rate has been reduced in the densest parts of models S7–S8 to the level at which it can no longer maintain large C^+ densities. Figure 7 illustrates the variations in the abundances of CO, C_2, and C^+ with depth into model S2, S4, S6, and S8. The column averaged densities for CH and CN follow the same trend as those for C_2, with CN probing somewhat denser regions of the cloud. The column-averaged densities for ^{13}CO are similar to, or slightly larger than those for ^{12}CO.

It is thus concluded that the column-averaged densities of CO can be up to a factor of 2–3 larger than those for C_2, *if* the densest part of the cloud is farthest removed from the radiation field. For these same models, the CO-averaged temperatures are lower. On the other hand, if a less dense part of the cloud is shielded from radiation, the CO averaged densities may be lower by a factor of 2, and the CO averaged temperatures higher by up to 15 K.

VI. CO LINE PROFILES

Inspection of the high-resolution spectra (Fig. 1) shows that the profiles for many translucent and high-latitude positions appear to differ significantly from a single Gaussian profile. They often show a double-peaked, asymmetrical structure, which is usually interpreted to indicate the presence of several closely spaced velocity components (see, e.g., Magnani, Blitz, and Wouterloot 1988). However, in many cases the ^{13}CO profile is single and peaks at a velocity in between those of the ^{12}CO maxima (e.g., HD 169454, HD 154368, HD 210121B2), so that alternative interpretations in terms of central reversals in an inhomogeneous medium appear more likely. Self-absorbed profiles are commonly seen toward warm GMCs, especially in higher frequency transitions (see, e.g., Snell and Loren 1977; Phillips *et al.* 1981; White *et al.* 1986), where they are thought to be produced by a cold region lying in front of a

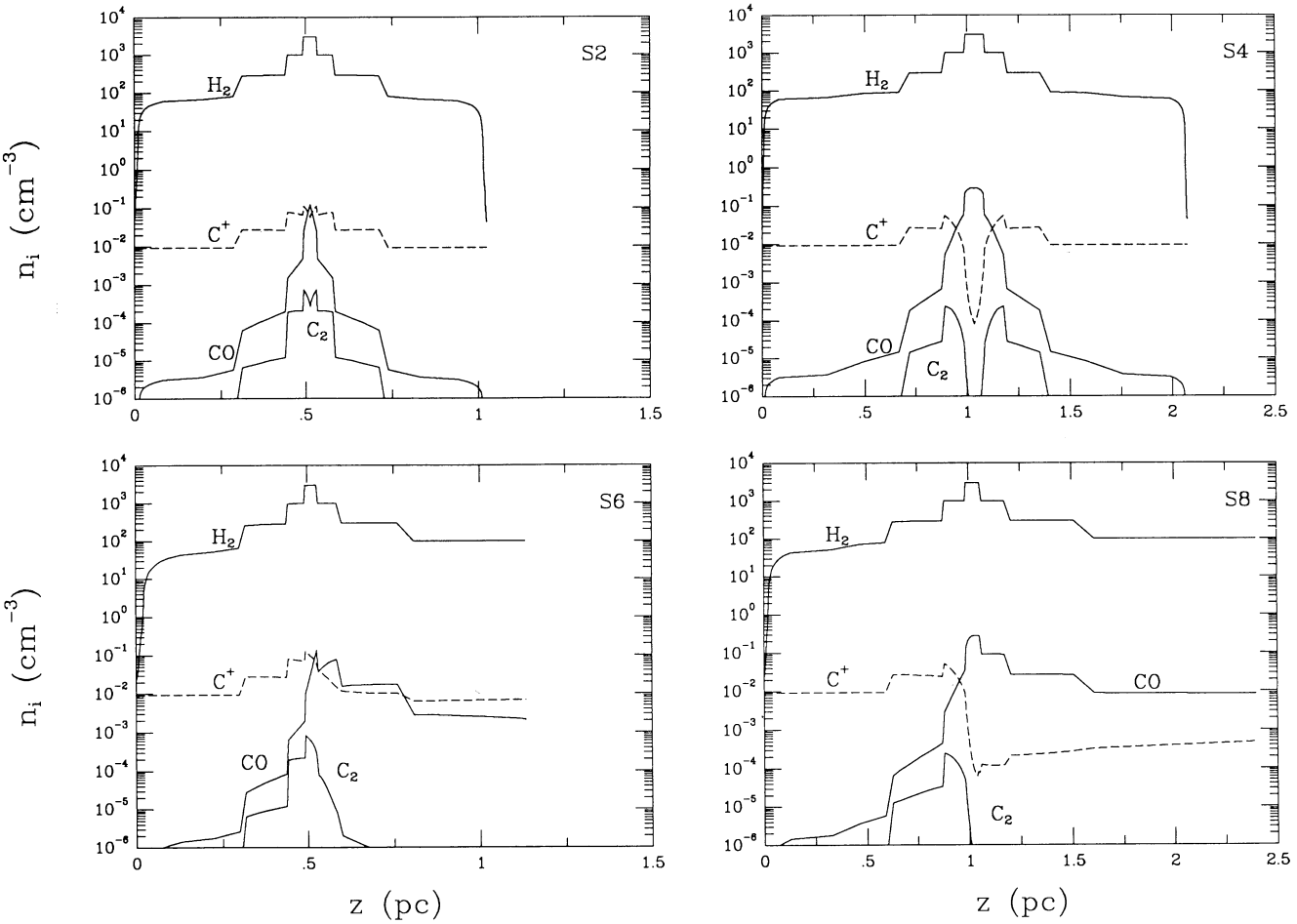

FIG. 7.—Variation of the H_2, CO, C_2, and C^+ abundances with depth in various cloud models described in the text. Models S2 and S4 with $A_V^{tot} = 1.5$ and 3 mag, respectively, have the radiation incident from both sides of the cloud and are thus symmetric with respect to the center. Models S6 and S8 have the radiation incident from one side only (at $z = 0$), but have otherwise the same physical parameters as models S2 and S4, respectively.

hot core. For the case of the externally illuminated translucent and high-latitude clouds, the situation is expected to be reversed, since the temperature is likely to decrease from the edge to the center. However, central reversals can arise in inhomogeneous atmospheres for a variety of reasons (Leung and Liszt 1976). We use theoretical models to illustrate how double-peaked profiles can readily occur, if the density and molecular abundance also vary with depth through a translucent cloud.

We consider as an example two of the models constructed by van Dishoeck and Black (1988*b*, 1989), i.e. models T3 and T4, whose gradients of temperature and density were constrained to satisfy a polytropic structure. The temperature varies from about 80 K at the edge to about 15–20 K in the center, whereas the density $n = n(\mathrm{H}) + n(\mathrm{H_2})$ varies from about 200 cm^{-3} at the edge to about 300–400 cm^{-3} in the center. The CO abundance is, of course, nearly zero at the edge and increases to a few times 10^{-5} to 10^{-4} in the centers of the clouds. Model T4 is thicker than T3 and thus has a greater central abundance of CO. These models specify all the variables, $n(\mathrm{H_2})$, T, $n(^{12}\mathrm{CO})$, and $n(^{13}\mathrm{CO})$, which govern the excitation and line formation of CO except for the velocity field. In the following, the original abundances of ^{12}CO and ^{13}CO in model T4 have been multiplied by a factor 0.75 at all depths. In order to solve the coupled equations of statistical equilibrium and radiative transfer and to compute line profiles, it is necessary to make critical assumptions about the velocity field. We have computed the excitation and line formation of CO in models T3 and T4 by three quite different methods. First, the radiative transfer was solved in terms of mean escape probabilities for the "equivalent" uniform cloud that has the same average density, average temperature, and column densities as the model. In this case, a single value of the linewidth, ΔV, is specified and all emergent profiles are, by definition of the escape probability, Gaussian functions such that $\int T_R\,dV = 1.0645 T_R\,\Delta V$. This is the same method of mean escape probabilities used to calculate the excitation as described in § IV*a*. The second conventional approach is to assume a systematic, large velocity gradient, dV/dR, and to solve the radiative transfer in the Sobolev approximation. The third technique presumes a microturbulent cloud characterized by a mean turbulent velocity, V_t. The computed profiles for ^{12}CO $J = 1 \rightarrow 0$ and ^{13}CO $J = 1 \rightarrow 0$ are shown in Figure 8. The velocity parameters have been selected so that the three different methods give the same integrated intensities in the ^{12}CO $J = 1 \rightarrow 0$ line. Values of $\Delta V = 0.7$ km s^{-1}, $dV/dR = 2.0$ km s^{-1} pc^{-1}, and $V_t = 0.7$ km s^{-1} yield $\int T_R(1 \rightarrow 0)dV = 3.5$ K km s^{-1} for model T3, while $\Delta V = 1.57$ km s^{-1}, $dV/dR = 1.35$ km s^{-1} pc^{-1}, and $V_t = 0.7$ km s^{-1} yield $\int T_R(1 \rightarrow 0)dV = 13.0$ K km s^{-1} for model T4. In the thicker model, T4, centrally reversed line profiles emerge naturally from either the Sobolev approximation or a microturbulent computation. These line profiles for idealized, symmetrical models are qualitatively similar in shape to observed profiles and have peak temperatures, $T_R(1 \rightarrow 0) \approx 6$–9 K, $T_R(3 \rightarrow 2) \approx 1.5$–2.5, and widths, $\Delta V \approx 1$–2 km s^{-1}, like those observed. The interpretations of the profiles are discussed separately for the different methods in the following paragraphs.

a) Sobolev Approximation

In the Sobolev (1960) method, the nonlocal radiative transfer is replaced by a piecewise local treatment, subject to the constraint that the velocity gradient dV/dR is large enough so that the thermalization length of photons

$$l_t \approx 0.22\left(\frac{28}{\mu}\right)^{1/2}\left(\frac{T_D}{30}\right)^{1/2}\left(\frac{dV}{dR}\right)^{-1} \text{ pc} \qquad (3)$$

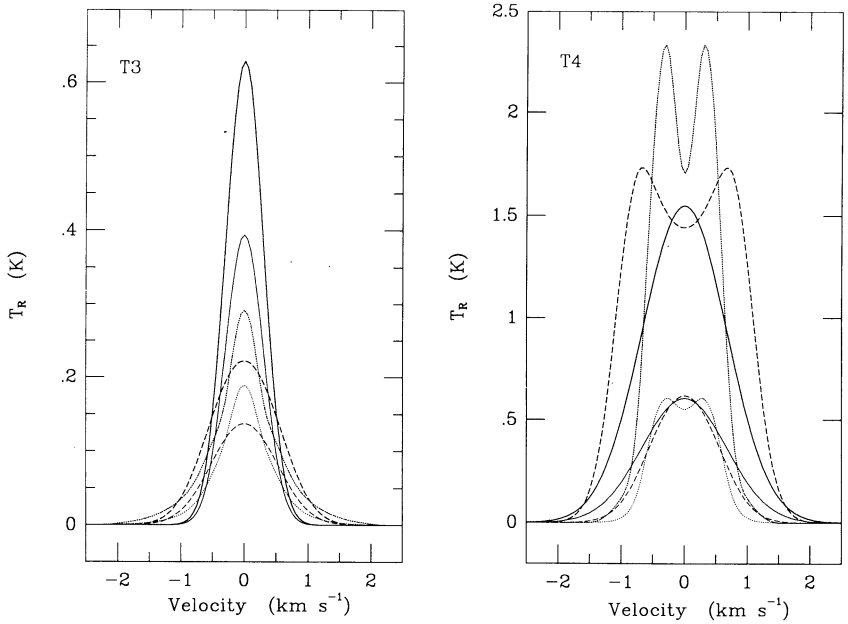

FIG. 8.—Theoretical profiles of ^{12}CO $J = 3 \rightarrow 2$ and ^{13}CO $J = 1 \rightarrow 0$ lines in translucent cloud models T3 and T4. In each case the solid curve is the Gaussian profile for the uniform equivalent model computed with mean escape probabilities. The dotted curve is the profile for the inhomogeneous model in the Sobolev approximation. The dashed curve is for the inhomogeneous model in the microturbulent approximation. The lower curve of each type is the ^{13}CO profile that corresponds to the stronger ^{12}CO $J = 3 \rightarrow 2$ line. The integrated intensities of the ^{12}CO $3 \rightarrow 2$ lines are $\int T_R\,dV = 0.47$, 0.29, and 0.30 K km s^{-1} in the mean escape, Sobolev, and microturbulent descriptions, respectively, for model T3; and 2.59, 2.78, and 3.79 K km s^{-1} for model T4. The corresponding integrated intensities for the ^{13}CO $J = 1 \rightarrow 0$ lines are 0.29, 0.18, and 0.18 in model T3, and 1.01, 0.76, and 0.82 K km s^{-1} in model T4.

is smaller than the radius of the cloud R_0, where μ is the molecular mass in atomic mass units, T_D is the local Doppler temperature, and dV/dR is in km s^{-1} pc^{-1}. The thermalization length is essentially the local mean free path.

Consider a spherical cloud of radius R_0, divided into concentric shells of thickness l_t. Each shell has a well-defined mean velocity $\bar{V}$ and a local velocity width δV. In the Sobolev approximation, photons created within a velocity interval δV about $\bar{V}$ (or equivalently, within the corresponding shell) are the only contributions to that part of the *emergent* line profile within δV about $\bar{V}$. Their escape is governed only by the optical depth and δV along that part of the viewer's line of sight through the particular shell of interest. The local width is usually taken to be the thermal Doppler width.

In the case of a completely uniform cloud, in which both the density, temperature, and CO abundance are constant with radius, each shell has the same thickness and contributes equally to the emergent profile. The extent of the profile is limited only by the total extent R_0 of the cloud and its corresponding extent in velocity. The resulting profile is rectangular. When the density or abundance of the emitting molecules varies with R, the profile can develop rounded shoulders. The different shells no longer have equal optical depths and excitation temperatures and thus no longer contribute the same intensity at each velocity. The degree to which the profile is peaked or flat-topped depends on how rapidly the optical depth and excitation fall off with R relative to the values for the innermost shells or shell. If the innermost shells are all optically thick at about the same excitation temperature, the profile will be flat-topped.

When both the density (or abundance) and temperature vary with R, centrally reversed profiles can arise. If the density decreases measured outward from the center of the cloud, and the temperature increases, then in the outer shells, a partial increase in excitation temperature T_{ex} can compensate for the decrease in optical depth and yield a net profile with a central reversal. Since the variations in abundance, temperature, and density need not be the same on the two sides of a real cloud, the true profile may appear asymmetric.

The temperature, density, and CO abundance variations from models T3 and T4 have been incorporated into a Sobolev code provided by P. R. Maloney (1987). In each shell, the CO excitation and optical depth were computed using exactly the same molecular data as described in § IV*a*. Double-peaked CO profiles, which resemble the observed profiles both in width and in strength, are readily produced in thick models such as model T4 for $dV/dR \approx 1$–3 km s^{-1} pc^{-1}. On the other hand, models of smaller total column density such as T3 usually produce single-peaked profiles. In order for double-peaked profiles to arise, the CO abundance must remain relatively constant in the center of the cloud before starting to drop to the outside, whereas the temperature must increase steadily with distance from the center.

The computed ratios of integrated line intensity are 1–0/3–2 = 12, 2–1/3–2 = 5.0, and 3–2/^{13}CO 1–0 = 1.6 for model T3 and 4.6, 2.8, and 3.7, respectively, for T4. The latter model produces line ratios similar to some of those observed (Table 7).

In a thick model such as T4, all carbon has been converted into CO in the center of the cloud, so that its abundance is relatively constant in the inner few shells. In model T3, however, the CO abundance has not yet reached its limiting value and continues to increase toward the center. If this picture is valid, it would provide additional support for the presence of temperature and density gradients in the clouds. It suggests that in cases where double-peaked profiles are observed, the CO abundance has probably reached its limiting value in the center of the cloud.

Clearly, this explanation does not apply to all cases where double-peaked or complicated line profiles are observed. For example, for the ζ Oph cloud, no reasonable single-component model can be constructed that reproduces the observed profiles, and it is plausible that two to four separate components are present in this case (Langer, Glassgold, and Wilson 1987; Le Bourlot, Gérin, and Pérault 1989). On the other hand, it may explain profiles such as observed for HD 169454 and HD 26571. An alternative interpretation has been put forward by Keto and Lattanzio (1989), in which double profiles are thought to arise from two colliding clouds or clumps. It would be interesting to investigate the influence of the temperature structure in the clouds on such models.

b) Microturbulent Approximation

The Sobolev approximation entailed specific presumptions about the velocity field that might be unrealistic. To test whether the profile shapes discussed above might be artifacts of that approximation, we have computed CO line profiles for radiative transfer in a microturbulent medium. For this purpose, we have used a code based on the work of Bernes (1978, 1979) that solves the coupled equations of statistical equilibrium and radiative transfer by a Monte Carlo method. In this case, the radiative transfer is explicitly nonlocal so that gradients in excitation might be expected to manifest themselves differently in the emergent line profiles than in the Sobolev approximation. For model T3, the microturbulent profiles are flat-topped, while for model T4, the profiles are centrally reversed and qualitatively similar to those computed in the Sobolev approximation. Again, we attribute the central reversal to excitation gradients that result from competing effects of outwardly increasing temperature and decreasing density and abundance. Photons near line center "see" preferentially the molecules of lower excitation.

The computed ratios of integrated line intensity, 1–0/3–2, 2–1/3–2, and 3–2/^{13}CO 1–0 are, respectively, 12, 5.1, and 1.7 for model T3, and 3.5, 1.4, and 4.6 for model T4. In comparison with the escape probability and Sobolev approximations, the microturbulent calculation yields a significantly smaller 1–0/3–2 ratio in model T4, one that is more typical of the observed values in Table 7. That is, the lines of higher excitation (e.g., $J = 3 \rightarrow 2$) are systematically stronger in the microturbulent treatment of model T4. This suggests a possible resolution of the discrepant densities inferred from the observed C_2 and CO lines, at least for clouds of higher total CO column density. If the CO excitation had been analyzed for inhomogeneous, microturbulent clouds, $J = 3 \rightarrow 2$ lines of the same strength would have been found to arise in regions of lower density than was inferred for homogeneous regions with line formation treated by mean escape probabilities.

These model studies suggest that full interpretation of millimeter and submillimeter line emission from translucent clouds may require detailed modeling of individual regions. It is a daunting possibility that conclusions about densities and isotope abundances from CO data can sometimes be distorted by the assumptions that are made about the structure and internal kinematics of these clouds. On the other hand, it is comforting to note that for clouds of lower total column

density, $N(CO) \leq 2 \times 10^{16}$ cm^{-2}, the different radiative transfer models give nearly identical results.

VI. CONCLUDING REMARKS

Significant improvements in recent years in telescopes and receivers at submillimeter wavelengths have made possible the detection of weak CO $J = 3 \rightarrow 2$ emission from translucent and high-latitude clouds. Comparison of the strength of these $3 \rightarrow 2$ lines with $1 \rightarrow 0$ and $2 \rightarrow 1$ emission can provide estimates of the densities in the clouds. These densities are typically found to be $n(H_2) \approx 1000$ cm^{-3}. Unfortunately, uncertainties in the calibrations and differences in beam sizes for the various lines prevent more accurate determinations at present.

The densities derived from the measured ^{12}CO $1 \rightarrow 0/3 \rightarrow 2$ and $3 \rightarrow 2/^{13}$CO $1 \rightarrow 0$ ratios have been compared with densities inferred from the C_2 absorption-line observations for translucent clouds. In general, the ^{12}CO $1 \rightarrow 0/3 \rightarrow 2$ and $2 \rightarrow 1/3 \rightarrow 2$ data result in densities that are higher by up to an order of magnitude than those found from the C_2 analysis. Several possible explanations for this discrepancy have been suggested, such as small-scale clumping, different distributions of CO and C_2 throughout the cloud, an overestimate of the C_2 collisional cross section, and an underestimate of the radiation field at $\lambda \approx 1$ μm. However, it remains difficult to explain simultaneously the relatively good agreement that is found between the densities obtained from the C_2 analysis and the ^{12}CO $3 \rightarrow 2/^{13}$CO $1 \rightarrow 0$ intensity ratios, in particular since the interpretation of the latter ratios is sensitive to the adopted ^{12}CO/^{13}CO abundance ratio and the relative distribution of the two species throughout the cloud. There is an indication that the densities inferred from CO lines sometimes depend on the assumptions about radiative transfer that are embedded in the excitation calculations, at least for the thicker translucent clouds. For these reasons, it would be better to limit the sample to clouds with $N(CO) \lesssim 10^{16}$ cm^{-2}. This is also the regime in which the largest sensitivity to density occurs. With slight improvements in receiver sensitivity and longer integration times, it should be possible to study these thinner clouds in more detail in the near future.

An important conclusion of this study is that the physical properties of the high-latitude clouds studied by Magnani, Blitz, and Wouterloot (1988) do not differ significantly from those inferred for the translucent clouds. A similar conclusion for some chemical properties was reached by de Vries and van Dishoeck (1988*a*) and is discussed in more detail by Gredel *et al.* (1990). Another interesting result is the very sensitive limit on the CO $J = 3 \rightarrow 2$ emission from the classical diffuse cloud toward ζ Oph, which excludes the higher density models of this region.

In the near future, it should be possible to improve significantly upon the analysis presented in this paper through ultraviolet observations of CO toward the stars with the Goddard High-Resolution Spectrograph on *Hubble Space Telescope*. Such measurements would provide direct information on the populations in the lower J levels from a single spectrum and would allow a more accurate determination of the CO column density toward the star. Since the same volume of the cloud is sampled, direct comparison with the densities derived from C_2 should be possible. At the same time, comparison of the CO excitation derived from the absorption-line observations compared with that found from the CO millimeter emission-line observations should give information on the small-scale structure of the clouds. The combination of CO absorption- and emission-line observations with C_2 absorption-line data should provide a powerful new tool to investigate the physical structure of diffuse and translucent clouds.

The authors are much indebted to the CSO staff, in particular to Antony Schinkel, for their continuous excellent support. They are grateful to E. C. Sutton and W. C. Danchi for making available their 345 GHz receiver for the initial observations, and for assistance during the first observing run. They are also indebted to E. Serabyn for the construction of the high-resolution AOS, to E. Falgarone for helpful discussions, and to the referee, E. R. Keto, for useful comments. The Caltech Submillimeter Observatory is supported by the National Science Foundation under grant AST 88-15132. The junctions were made at AT&T Bell Laboratories by R. E. Miller. J. H. B. thanks NASA for support through grant NAGW-763 to the University of Arizona and is grateful to P. R. Maloney for providing his radiative transfer codes.

REFERENCES

Bernes, C. 1978, *Stockholm Observatory Report*, No. 15.
———. 1979, *Astr. Ap.*, **73**, 67.
Black, J. H., and Dalgarno, A. 1977, *Ap. J. Suppl.*, **34**, 405.
Black, J. H., and van Dishoeck, E. F. 1990, *Ap. J. (Letters)*, submitted.
———. 1991, in preparation.
Blitz, L., Magnani, L., and Wandel, A. 1988, *Ap. J. (Letters)*, **331**, L127.
Cardelli, J. A., Suntzeff, N. B., Edgar, R. J., and Savage, B. D. 1990, *Ap. J.*, in press.
Chu, S.-I., and Dalgarno, A. 1975, *Proc. Roy. Soc. A*, **342**, 191.
Crane, P., Hegyi, D. J., Kutner, M. L., and Mandolesi, N. 1989, *Ap. J.*, **346**, 136.
Crutcher, R. M. 1985, *Ap. J.*, **288**, 604.
Crutcher, R. M., and Federman, S. R. 1987, *Ap. J. (Letters)*, **316**, L71.
Crutcher, R. M., and Watson, W. D. 1981, *Ap. J.*, **244**, 855.
Danks, A. C., and Lambert, D. L. 1983, *Astr. Ap.*, **124**, 188.
de Vries, C. P., and van Dishoeck, E. F. 1988*a*, *Astr. Ap.*, **203**, L23.
———. 1988*b*, *Messenger*, **53**, 47.
———. 1990, in preparation.
Draine, B. T. 1978, *Ap. J. Suppl.*, **36**, 595.
Drdla, K., Knapp, G. R., and van Dishoeck, E. F. 1989, *Ap. J.*, **345**, 815.
Ellison, B. N., Schaffer, P. L., Schaal, W., Vail, D., and Miller, R. E. 1989, *Int. J. Infrared Millimeter Waves*, **10**, 937.
Falgarone, E., and Phillips, T. G. 1990, *Ap. J.*, **359**, 344.
Flower, D. R., and Launay, J. M. 1985, *M.N.R.A.S.*, **214**, 271.
Gredel, R., and Münch, G. 1986, *Astr. Ap.*, **154**, 336.
Gredel, R., van Dishoeck, E. F., and Black, J. H. 1990, in preparation.
Gredel, R., van Dishoeck, E. F., de Vries, C. P., and Black, J. H. 1990, in preparation.
Hawkins, I., and Jura, M. 1987, *Ap. J.*, **317**, 926.
Hobbs, L. M., Black, J. H., and van Dishoeck, E. F. 1983, *Ap. J. (Letters)*, **271**, L95.
Hobbs, L. M., Blitz, L., and Magnani, L. 1986, *Ap. J. (Letters)*, **306**, L109.
Hobbs, L. M., Blitz, L., Penprase, B. E., Magnani, L., and Welty, D. E. 1988, *Ap. J.*, **327**, 356.
Jannuzi, B. T., Black, J. H., Lada, C. J., and van Dishoeck, E. F. 1988, *Ap. J.*, **332**, 995.
Joseph, C. L., Snow, T. P., Seab, C. G., and Crutcher, R. M. 1986, *Ap. J.*, **309**, 771.
Keto, E. R., and Lattanzio, J. C. 1989, *Ap. J.*, **346**, 184.
Keto, E. R., and Myers, P. C. 1986, *Ap. J.*, **304**, 466.
Knapp, G. R., and Bowers, P. F. 1988, *Ap. J.*, **331**, 974.
Kutner, M. L., and Ulich, B. L. 1981, *Ap. J.*, **250**, 341.
Lada, E. A., and Blitz, L. 1988, *Ap. J. (Letters)*, **326**, L69.
Langer, W. D., Glassgold, A. E., and Wilson, R. W. 1987, *Ap. J.*, **322**, 450.
Le Bourlot, J., Gérin, M., and Pérault, M. 1989, *Astr. Ap.*, **219**, 279.
Letzelter, C., Eidelsberg, M., Rostas, F., Breton, J., and Thieblemont, B. 1987, *Chem. Phys.*, **114**, 273.
Leung, C. M., and Liszt, H. S. 1976, *Ap. J.*, **208**, 732.
Magnani, L., Blitz, L., and Mundy, L. 1985, *Ap. J.*, **295**, 402.
Magnani, L., Blitz, L., and Wouterloot, J. G. A. 1988, *Ap. J.*, **326**, 909.
Maloney, P. R. 1987, Ph.D. thesis, University of Arizona.
Masson, C. R. 1982, *Astr. Ap.*, **114**, 270.
Mathis, J. S., Mezger, P. G., and Panagia, N. 1983, *Astr. Ap.*, **128**, 212.
Penprase, B. E., Blades, J. C., Danks, A. C., and Crane, P. 1990, *Ap. J.*, in press.
Penzias, A., and Burrus, C. A. 1973, *Ann. Rev. Astr. Ap.*, **11**, 51.

Phillips, T. G., Knapp, G. R., Huggins, P. J., Werner, M. W., Wannier, P. G., Neugebauer, G., and Ennis, D. 1981, *Ap. J.*, **245**, 512.
Schinke, R., Engel, V., Buck, U., Meyer, H., and Diercksen, G. H. F. 1985, *Ap. J.*, **299**, 939.
Sellgren, K., Werner, M. W., and Dinerstein, H. L. 1983, *Ap. J.* (*Letters*), **271**, L13.
Snell, R. L., and Loren, R. B. 1977, *Ap. J.*, **211**, 122.
Sobolev, V. V. 1960, *Moving Envelopes of Stars* (Cambridge, Mass.: Harvard University Press).
Stahl, O., Wilson, T. L., Henkel, C., and Appenzeller, I. 1989, *Astr. Ap.*, **221**, 321.
Stark, G., Smith, P. L., Yoshino, K., Ito, K., and Parkinson, W. H. 1990, in preparation.
Stutzki, J., Stacey, G. J., Genzel, R., Harris, A. I., Jaffe, D. T., and Lugten, J. B. 1988, *Ap. J.*, **332**, 379.
Sutton, E. C., Danchi, W. C., Jaminet, P. A., and Masson, C. R. 1990, *Ap. J.*, **348**, 503.
Turner, B. E., Rickard, L. J, and Lan-ping, X. 1989, *Ap. J.*, **344**, 292.
van Dishoeck, E. F. 1990, in *The Evolution of the Interstellar Medium*, ed. L. Blitz (*A.S.P. Conf. Ser.*), in press.
van Dishoeck, E. F., and Black, J. H. 1982, *Ap. J.*, **258**, 533.
———. 1986*a*, *Ap. J. Suppl.*, **62**, 109.
———. 1986*b*, *Ap. J.*, **307**, 332.
van Dishoeck, E. F., and Black, J. H. 1988*a*, in *Rate Coefficients in Astrochemistry*, ed. T. J. Millar and D. A. Williams (Dordrecht: Kluwer), p. 209.
———. 1988*b*, *Ap. J.*, **334**, 771.
———. 1989, *Ap. J.*, **340**, 273.
van Dishoeck, E. F., and de Zeeuw, T. 1984, *M.N.R.A.S.*, **206**, 383.
Viala, Y. P. 1986, *Astr. Ap. Suppl.*, **64**, 391.
Viala, Y. P., Letzelter, C., Eidelsberg, M., and Rostas, F. 1988, *Astr. Ap.*, **193**, 265.
Viala, Y. P., Roueff, E., and Abgrall, H. 1988, *Astr. Ap.*, **190**, 215.
Welty, D. E., Hobbs, L. M., Blitz, L., and Penprase, B. E. 1989, *Ap. J.*, **346**, 232.
White, G. J., Phillips, J. P., Richardson, K. J., and Horton, R. H. 1986, *Astr. Ap.*, **159**, 309.

JOHN H. BLACK: Steward Observatory, University of Arizona, Tucson, AZ 85721

R. GREDEL: I. Physikalisches Institut der Universität zu Köln, Zülpicher Strasse 77, 5000 Köln 41, Germany

T. G. PHILLIPS: Downs Laboratory of Physics, California Institute of Technology 320-47, Pasadena, CA 91125

EWINE F. VAN DISHOECK: Sterrewacht Leiden, P.O. Box 9513, 2300 RA Leiden, The Netherlands